A Framework for Validation and Testing of a CubeSat Retarding Potential Analyzer

Stephen E. Noel

Thesis submitted to the Faculty of the
Virginia Polytechnic Institute and State University
in partial fulfillment of the requirements for the degree of

Master of Science
in
Aerospace Engineering

Gregory D. Earle, Chair
Craig Woolsey
Kevin Shinpaugh

August 6, 2015
Blacksburg, Virginia

Keywords: Space Plasma, Ion Energy Spectrum, Calibration, Retarding Potential Analyzer, Spacecraft

A Framework for Validation and Testing of a CubeSat Retarding Potential Analyzer

Stephen E. Noel

(ABSTRACT)

Traditionally, Retarding Potential Analyzers (RPAs) operate exclusively on large satellites due to the size, power, and mass constraints posed by nano-satellites like CubeSats. These sensors take *in-situ* measurements of Earth's atmospheric ion current during a range of time-varied "retarding" voltage steps. Curve-fitting the retarding voltage versus collected current data provides derived measurements of ion density, ram velocity, and temperature. In order to successfully miniaturize these instruments and validate their performance prior to launch, thorough calibration and comprehensive end-to-end testing must be performed. This paper discusses the difficulties of performing complete system validation in ground-based vacuum chamber testing for RPAs. A procedure for RPA instrument calibration will be presented along with the calibration results for the Lower Atmosphere/Ionosphere Coupling Experiment (LAICE) CubeSat RPA. This paper presents a user-friendly and robust software control suite developed to read, parse, and interpret the data from the LAICE RPA. Electronics noise testing and analysis defines the performance boundaries of the instrument electronics. End-to-end testing of the LAICE RPA with a hot-filament ion source simulating the space plasma verifies the function of the LAICE RPA sensor and electronics, as well as the software control, thus qualifying the instrument for on-orbit use.

Dedication

To my father, Robert Noel II, for his inspiration and unconditional guidance.

To my grandparents, Doris Noel, Robert Noel I, Rita Thornton, and William Thornton for their support and for teaching me the value of work ethic and discipline.

Acknowledgments

I would like to thank the Virginia Space Grant Association for supporting my research through the Graduate STEM Research Fellowship Program. I would also like to give special thanks to Dr. Greg Earle, Chad Fish, and Dr. Ryan Davidson for their invaluable guidance and mentorship on this project. My thesis was built upon the previous work of many people including Lucy Fanelli, Dr. Ryan Davidson, and Dr. Robbie Robertson, and they deserve many thanks for setting the groundwork for the testing and calibration explained here. This paper could not have been completed without the contributions of Lee Kordella's focused and relentless assistance in hardware debugging and sub-system testing but also Vidur Garg and Namitha Somasundaram's expertise in digital electronics and FPGA software.

Funding for this research provided by the National Science Foundation (AGS-1242898).

Unless otherwise noted, all photos by author, 2015.

Contents

List of Figures

List of Tables

List of Acronyms

ADC Analog to Digital Converter

COTS Commercial Off-The-Shelf

ELaNa NASA Educational Launch of Nanosatellites

FPGA Field Programmable Gate Array

GUI Graphical User Interface

ISS International Space Station

LAICE Lower Atmosphere/Ionosphere Coupling Experiment

LEO Low Earth Orbit

LSB Least Significant Bit

MSB Most Significant Bit

NSF National Science Foundation

PCB Printed Circuit Board

PI Principal Investigator

PPS Points Per Sweep

RG Retarding Grid

RPA Retarding Potential Analyzer

RV Retarding Voltage

sub-VI Virtual Instrument function

TDMS Technical Data Management Structure

VI Virtual Instrument

Chapter 1

Introduction

The Lower Atmosphere/Ionosphere Coupling Experiment (LAICE) satellite will be the first Earth satellite to exclusively investigate the energy and momentum transfer of gravity waves produced by low-atmosphere weather systems to the mesosphere, lower thermosphere, and ionosphere. The satellite will also be one of the first 6U CubeSats used for space science. The LAICE team includes scientists and students at Virginia Tech and the University of Illinois, and is funded by the National Science Foundation (NSF). The expected launch date is August 2016 through the NASA Educational Launch of Nanosatellites (ELaNa) program. The LAICE CubeSat will be deployed from the International Space Station (ISS) into a near circular orbit between 350 and 450 km, depending on the altitude of the ISS at the time of release.

The two main goals of LAICE are the systematic observation of gravity waves and the mapping of active gravity wave regions in the ionosphere over multiple seasons and times. The desired mission duration of approximately nine months provides adequate longitudinal and local time coverage over different seasons. By mapping active gravity wave regions, the data will be used to validate and improve the current gravity wave models of the Earth. Systematic observation of primary and secondary gravity waves will lead to more accurate tracing of the sources of these waves. Both of these goals will help describe the propagation of lower atmospheric waves into higher-altitude regions. The hope is that LAICE will lend novel data to the understanding of the energy exchange between these atmospheric regions. Figure 1.1 displays a rendering of the LAICE CubeSat.

CubeSats are a class of nano-satellites that use standardized architectures and Commercial Off-The-Shelf (COTS) parts to reduce cost, providing affordable access opportunities to universities and scientists. These missions allow the greater scientific community to fly more experiments when integrating with a large research satellite is cost-prohibitive, or when the experiment can be conducted with smaller-scale hardware and support systems. Standard CubeSat sizes are referred to in "U's" or "units" measuring roughly a 10x10x10 cm volume. LAICE follows the "6U" CubeSat form factor, or roughly a 30x20x10 cm volume.

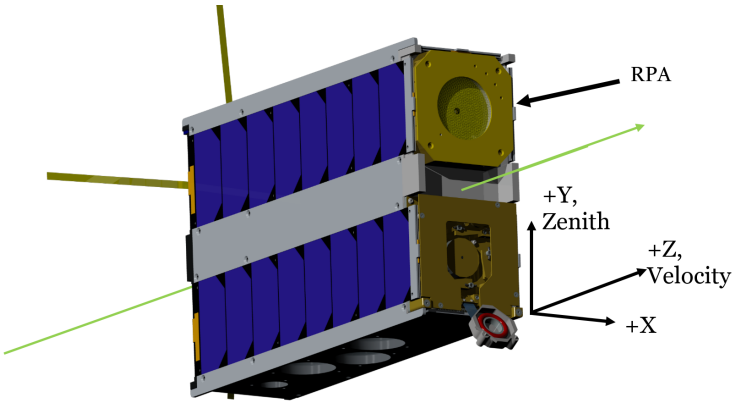

Figure 1.1: **LAICE CubeSat flight orientation with the starboard solar panels illuminated by the Sun.** The green vector highlights the satellite's orbit path. The RPA sensor faces toward the ram direction on the zenith-bow side of LAICE.

Retarding Potential Analyzers (RPAs) have been used on many satellite missions since the mid-20th century (Hanson et al., 1981), but have never been flown on a CubeSat because previous designs haven't been compatible with the power, mass, size, and attitude constraints imposed by the standard CubeSat design. The LAICE RPA has been developed by a team at Virginia Tech over the past few years with the end goal of designing a CubeSat-compatible RPA. Figure 1.2a shows the assembled LAICE RPA sensor and Figure 1.2b shows the electronics board assembly.

The LAICE RPA will collect *in-situ* measurements of ion density and temperature in the ionosphere. The RPA technique is well documented in literature (Knudsen, 1966; Hanson et al., 1981; Zuccaro and Holt, 1982; Kil and Heelis, 1998; Klenzing et al., 2008; Davidson and Earle, 2011) and therefore will not be discussed in detail here. The ultra-low current signals expected on orbit (as low as 100 pA) necessitate careful calibration of the LAICE RPA sub-system. EMI shielding and selection of low-noise support equipment ensures precise calibration of the LAICE RPA. Instrument validation requires end-to-end testing as well as sensitivity testing of the full instrument assembly. These tests require a simulated plasma environment, which is generated using a hot-filament ion source. For sensitivity testing the generated ion beam properties will be adjusted by varying the ion energy and ion density inside the vacuum chamber. This will allow us to monitor how the I-V characteristic reacts to changes in the simulated plasma.

The LAICE RPA requires user-friendly and robust software control using a suite of programs to read, parse, and interpret the data. This allows users to calibrate the RPA, perform noise floor analysis, and conduct end-to-end validation testing. The milestones of LAICE RPA validation are outlined below.

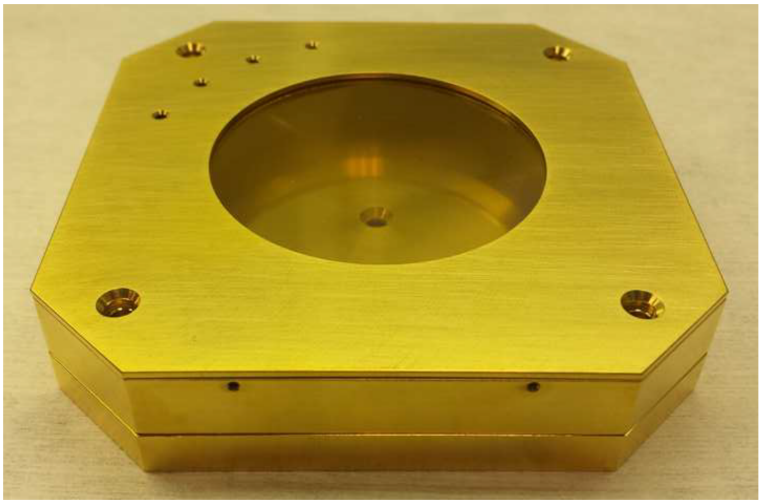

(a) RPA Sensor

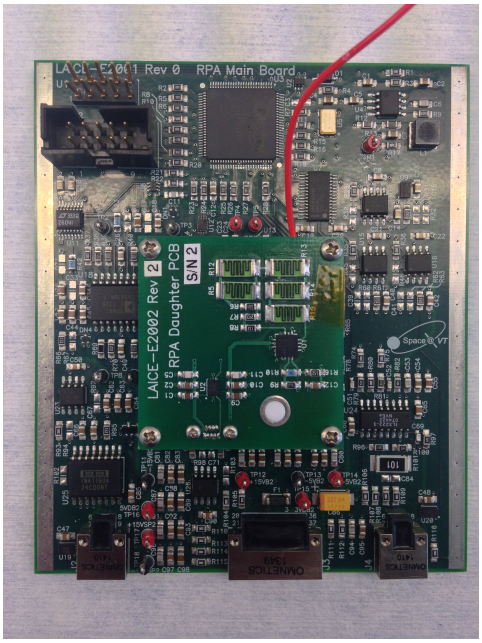

(b) RPA Boards

Figure 1.2: **LAICE RPA sensor with prototype main board and daughter board assembly.** RPA Sensor shown on 1.2a and RPA prototype boards on 1.2b. Figure 1.2a photograph taken by Gregory Earle.

Objectives:

1. Develop a control code and Graphical User Interface (GUI) for the LAICE RPA.
2. Calibrate the LAICE RPA electronics and present the procedure, calibration curve results, and goodness-of-fit evaluation for each regression.
3. Conduct noise analysis for the LAICE RPA electronics suite.
4. Generate an I-V characteristic using an ion source to validate end-to-end functionality of the LAICE RPA instrument.
5. Perform neutral density and ion beam energy sensitivity tests on the subsystem and present the results.

Chapter 2

Literature Review

2.1 LAICE RPA Instrument

The LAICE RPA will be the first RPA to fly on a CubeSat (Fanelli et al., 2016). Figure 2.1 shows a high-level flowchart of an RPA system. The sensor is made up of conductive mesh grids stacked parallel to each other and a grounded collector plate with which the electronics suite measures the absorbed ion current.

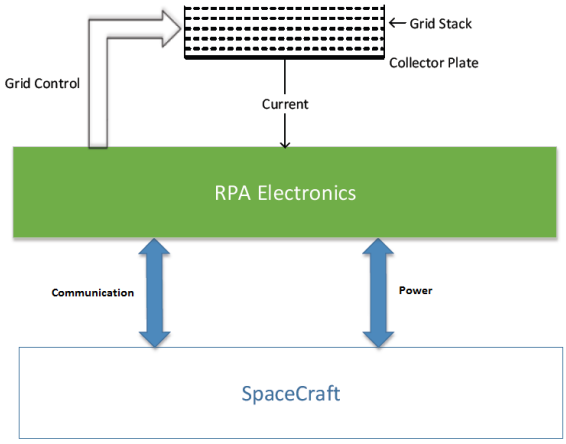

Figure 2.1: **Flowchart of an RPA instrument.** Electronics boards provide the required voltages to the grids and amplify, read, and digitize the current data from the collector plate. Lucy Fanelli. *Electronics for a versatile and robust retarding potential analyzer for use in nano-satellite platforms.* 2014. Masters thesis, Virginia Tech. Used under fair use, 2015.

Figure 2.2 shows an exploded rendering of the LAICE RPA sensor. The series of gold electroformed grids is aligned normal to the ram direction of the satellite, and each of the grids is individually biased to certain potentials in order to repel incoming photo-electrons and

allow ions of specific energies to reach the collector plate. In the LAICE RPA, five grids are used to accomplish this. The outermost grid ("Aperture Grid 1") is held at ground to prevent the interior electric field from affecting the incoming ions, while the next grid in the stack ("Aperture Grid 2/Retarding Grid 1") can be held at ground or swept at a range of electric potentials. The "Retarding Grid 2" (or RG) mesh gets biased over one second to a range of voltages from 0-12 V in order to set an energy barrier for the incoming ions. This is referred to as a sweep. Sweeping the RG potential changes the energy barrier and therefore the amount of ions absorbed by the collector. For instance, if the RG is set at ground, all incoming ions will pass through the grid and register as a current on the collector plate. If the RG is set to a non-zero potential it will repel all ions with a lower energy than the swept potential. During the operation of the RPA this grid is swept from 0-12 V and the current at the collector is measured using a logarithmic electrometer at each discrete potential. The collected ion current and voltage steps are the primary science data sent out from the LAICE RPA. The next grid in the stack, the "Shield Grid," is also grounded to the sensor chassis. The "Suppressor Grid," last in the stack of grids, is held at a constant -12 V to prevent incoming photo-electrons from reaching the collector, and also to contain secondary-electrons produced by ion impact or photoelectrons at the collector. Additional information on the design and theory of the LAICE RPA is available in Fanelli (2014).

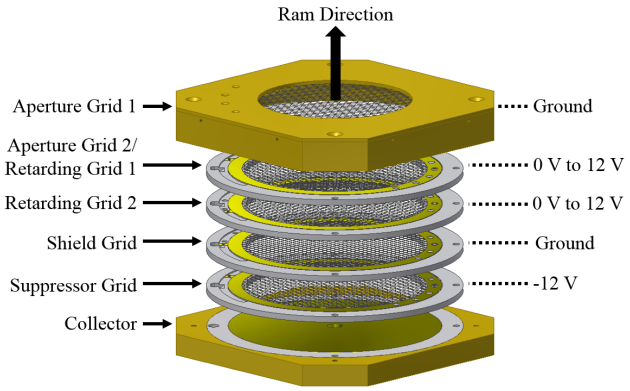

Figure 2.2: **LAICE RPA sensor mechanical assembly.** This CAD model shows an exploded view of the RPA sensor and defines the name of each mesh grid. Machined Kel-F spacers surround the inner grids, providing insulation and a groove to hold the grids in position. Fanelli, L., S. Noel, et al. (2016). A versatile retarding potential analyzer for nano-satellite platforms. Review of Scientific Instruments. Manuscript submitted for publication. Used under fair use, 2015.

At the bottom of the RPA sensor is the collector plate. This grounded surface collects the incoming ions and the resulting current is read by a logarithmic trans-impedance amplifier (Texas Instruments LOG114 electrometer) in the RPA control circuit. Great care has been taken to isolate this connection and minimize leakage currents. The current read from the collector along with the retarding grid voltage at each sample interval are the most critical pieces of data generated by the RPA. When plotted together, this set of data is referred

to as an I-V (current-voltage) plot with RG voltage represented on the x-axis and collector current on the y-axis. Figure 2.3 shows an idealized RPA I-V curve in a multi-constituent plasma with the individual idealized I-V curves of its constituents. All three species have the same density and temperature in this example.

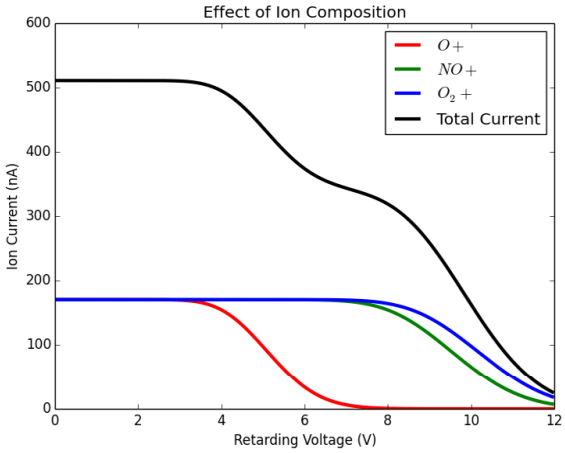

Figure 2.3: **Example idealized curves of varying ion composition and composite I-V curve.** As the retarding voltage inside the RPA increases, the ion current decreases because low-energy ions are repelled before impacting the collector plate. The red, green, and blue lines show theoretical I-V curves for particular plasma constituents, while the black line demonstrates an ideal I-V curve, which is a superposition of the individual I-V curves. The black "Total Current" line shape is more likely to be seen on orbit where a mixture of ambient gaseous particles exists. Fanelli, L., S. Noel, et al. (2016). A versatile retarding potential analyzer for nano-satellite platforms. Review of Scientific Instruments. Manuscript submitted for publication. Used under fair use, 2015.

The LAICE RPA will be used in conjunction with another instrument to detect gravity waves. The LAICE RPA will collect high fidelity measurements compared to previous missions because of the on-orbit oversampling and averaging capabilities of the on-board FPGA (Westerhoff et al., 2015). Table 2.1 shows the simulated measurement performance of the LAICE RPA. Relating these science requirements to engineering requirements is a difficult and inexact task. Quantifying the actual error in the density, temperature, and velocity measurements is usually left to simulation rather than lab testing. Tracing errors in the RPA electrometer output to these parameters would involve taking the instrument calibration offsets and noise study results and constructing a few sets of sample RPA data that incorporate the characterized relative error along the sweep. These curves would then need to be curve-fit using a Levenberg-Marquardt algorithm and compared to the error-free cases. Only then would one be able to tie the engineering capabilities of the instrument back to its specified science requirements. This is beyond the scope of this study, but a streamlined technique like this could prove useful for future designs. A characterization of instrument sensitivity to the

Table 2.1: **Expected RPA measurement performance.** The expected performance capabilities of the LAICE RPA presented here will be confirmed via instrument sensitivity testing and subsequent error tracing back to science requirements. (Westerhoff et al., 2015)

Measurement	**Sensitivity**	**Dynamic Range**	**Accuracy**
Ion density	300 cm^{-3}	300 - 5×10^7 cm^{-3}	$\pm 5\%$
Ion temperature	100 K	$500 - 3000$ K	± 5 K
Light/Heavy Ion Composition	$\pm 10\%$	$10 - 100\%$	$\pm 10\%$

noise level will suffice for the LAICE mission according to the LAICE Principal Investigators (PIs).

Chapter 3

Methods and Apparatus

3.1 RPA Software

Figure 3.1 shows a flowchart of the LAICE RPA instrument. The LAICE RPA electronics suite consists of two printed circuit boards (PCBs). The "RPA Main Board" handles analog-to-digital conversion, housekeeping data sampling, command interpretation, data transmission, and biasing of the RPA instrument grids. The "RPA Daughter Board" houses the Texas Instruments logarithmic amplifier which takes the current read from the sensor collector plate and converts it to an analog voltage signal. This output signal gets sent to the "RPA Main Board" for amplification, filtering, and digital conversion before being packetized and sent to the flight computer via RS-422 serial protocol. Fanelli (2014) details the design of the LAICE RPA's hardware and FPGA software.

The LAICE RPA requires a packet of five bytes via RS-422 protocol containing uplink commands. Figure 3.2 defines the RPA command uplink packet controllable modes by byte. The packet begins with a start byte followed by four command bytes specifying the sweep mode of the RPA. Figure 3.3 defines all of the possible commands by bit representation. These commands enter the RS-422 transceiver Most Significant Bit (MSB) first. Each command byte must be sent with a valid value for the RPA to accept the command.

The instrument boards send back a variable-length packet depending on the "points per sweep" mode of the sweep performed. In the 128 points per sweep mode, for instance, the RPA returns 23 bytes of housekeeping data, 512 bytes of RPA data, and one end word byte. The RPA sends its data values (RG voltage and ion current) in alternating 16-bit words per time step. Figure 3.4 defines the downlink packet and specifies the number of bits and bytes expected in each mode.

The LAICE RPA was designed to communicate with the spacecraft data handler board via RS-422 protocol. For lab testing, the RPA requires a software interface to receive commands and send back housekeeping and science data using its serial port. Using the RPA GUI, the user

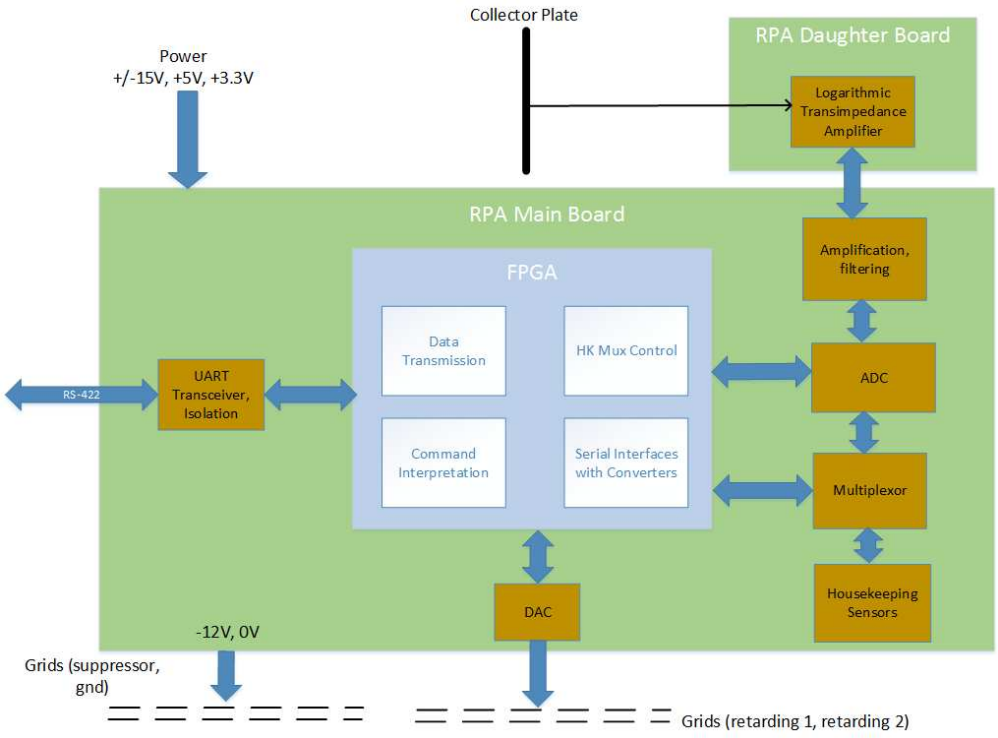

Figure 3.1: **LAICE RPA instrument flowchart.** RPA instrument main board (center) holds the FPGA, ADC, and amplification circuit as well as the grid biasing circuit. The daughter board houses the high-precision Texas Instruments logarithmic amplifier which converts the sensitive collector current into a voltage output signal. Lucy Fanelli. *Electronics for a versatile and robust retarding potential analyzer for use in nano-satellite platforms.* 2014. Masters thesis, Virginia Tech. Used under fair use, 2015.

LAICE RPA Board Command Definition			
Order in Packet	Bit Name	Acronym	bits (all per sec)
RPA	Start Word RPA	EWR	8
	Step Size		16
	Pts per Sweep	PpS	8
	zero padding		5
	RG2 Mode		1
	Sweep Mode		2
	Total		40

Figure 3.2: **RPA command bit definitions.** The LAICE RPA accepts a packet of five bytes via RS-422 protocol containing uplink commands. This packet consists of a start byte followed by four bytes specifying the next sweep mode of the RPA.

to RPA	
Start Word RPA Value	Bit
Start Word RPA	1000011
Step Size Value OR RG Voltage	Bit
Step Size or RG Voltage MIN (in counts)	00000000 00000000
Step Size or RG Voltage MAX (in counts)	11111111 11111111
Points per Sweep Value	Bit
32	00100000
64	01000000
128	10000000
RG2 Mode Value	Bit
Swept	0
Ground	1
Sweep Mode Value	Bit
Constant stepping	00
Constant Value at D/A	01
Smart Sweep	10

Figure 3.3: **RPA command bit-specific definitions.** The LAICE RPA accepts five mode commands using four bytes of uplink commands. These commands enter the RS-422 transceiver MSB-first. Each command byte must be sent with a valid value for the RPA to accept the command.

LAICE RPA Board Generated Telemetry				
Mode		32 sps	64 sps	128 sps
Order in Packet	Bit Name	bits (all per sec)	bits (all per sec)	bits (all per sec)
1	Start Word RPA	8	8	8
2	Step Size	16	16	16
3	Pts per Sweep	8	8	8
4	zero padding	5	5	5
5	RG2 Mode	1	1	1
6	Sweep Mode (RGMode)	2	2	2
7	Temp Monitor 1 RPA	16	16	16
8	Temp Monitor 2 RPA	16	16	16
9	Temp Monitor 3 RPA	16	16	16
10	Temp Monitor DB RPA	16	16	16
11	15V Monitor RPA	16	16	16
12	5V Monitor RPA	16	16	16
13	3.3V Monitor RPA	16	16	16
14	RG2 Grid Monitor RPA	16	16	16
15	SG Grid Monitor RPA	16	16	16
16	RPA Data	1024	2048	4096
17	End Word RPA	8	8	8
	RPA Total	1216	2240	4288

Figure 3.4: **RPA downlink bit definitions.** The LAICE RPA sends a variable-length packet depending on the "points per sweep" mode of the sweep performed. In the 128 points per sweep mode, for instance, the RPA returns 23 bytes of housekeeping data, 512 bytes of RPA data, and one end word byte. The RPA sends its data values (RG voltage and ion current) in alternating 16-bit words per time step. The bit name section highlighted in blue references the "echoed" command packet sent to the RPA to initialize the sweep.

can easily select what COM port the instrument is plugged into and start communicating within seconds. A flow chart of the RPA GUI can be found in Figure 3.5. The control code for the LAICE RPA and its associated sub-programs were programmed with National Instruments LabView software.

The RPA requires a binary start word followed by four command bytes that specify which sweep mode to initiate. The GUI software takes user-readable commands then generates and sends the appropriate binary commands to the RPA. Every time the RPA receives a command, it will perform a sweep, packetize the data, and send its data packet back to the control interface within one second. The GUI has additional functionality which allows the user to save each packet of data into a unique and user-readable file. External test equipment control for calibration and end-to-end testing are also built into the GUI. Figure 3.6 shows the RPA GUI software block diagram with its data flow to external instruments. The GUI can communicate and control the Keithley 6220 Precision Current Source and the Lesker KJL4500 Ion Gauge Controller for calibration or end-to-end testing. Using various sub-programs (described in Appendix A) the GUI communicates with the RPA, applies engineering coefficients to the science and housekeeping data, and outputs the parsed data to a file and on-screen.

The front panel of the GUI can be seen in Figure 3.7. Users have multiple options on how often to prompt the RPA to take a measurement, where the output data is saved, and whether they would like the GUI to read and store the latest pressure reading inside the chamber from an (optional) ion gauge. The code updates the visualized housekeeping monitors and the latest I-V curve for each received downlink packet. The "Run Counter" indicator updates with each run as well. "Sample Period" control can be set to any integer time value in seconds, provided that the time is greater than one second. The "Output File Initialization" controls allow the user to select the file path of the output file as well as other test notes to include in the output file. The notes feature is especially useful when sampling the RPA at frequent time intervals and an anomaly or interesting data feature occurs during testing which the user wants to note in the output data file. To initiate a sweep, the "Run RPA" button should be pressed, and to stop sweeping the "Stop RPA" button should be selected. While the GUI executes, the user has a few options for control during the test:

1. Change the RPA mode.
2. Stop the program or the sweep.
3. Start or stop saving output files.
4. Add test notes to the output file.

RPA mode controls can be found in the upper left corner of the GUI. A close-up of the mode controls can be seen in Figure 3.8. This "RPA Command" LabView control cluster allows the user to easily select the RPA mode via drop-down menus for each option. This

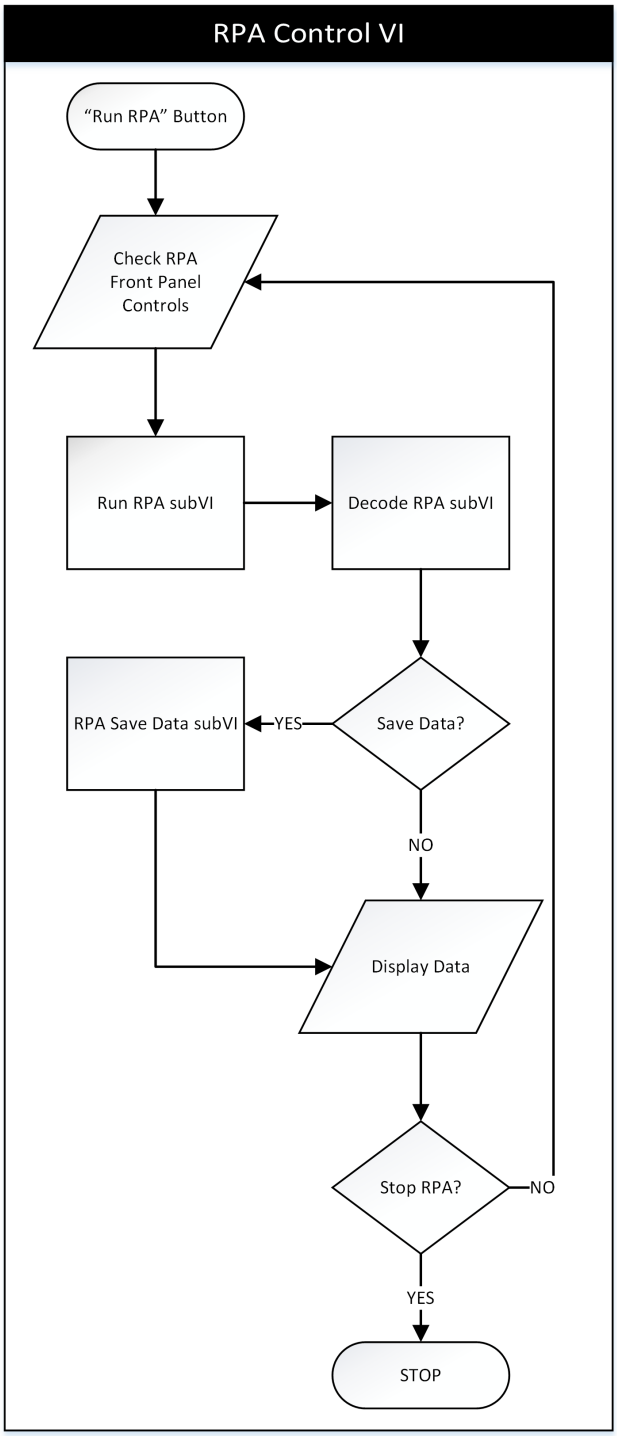

Figure 3.5: **RPA control code software flowchart.** The RPA control VI handles the commanding of the RPA as well as data parsing, output file generation, GUI processing, timing of RPA commands, and ion gauge command and data collection.

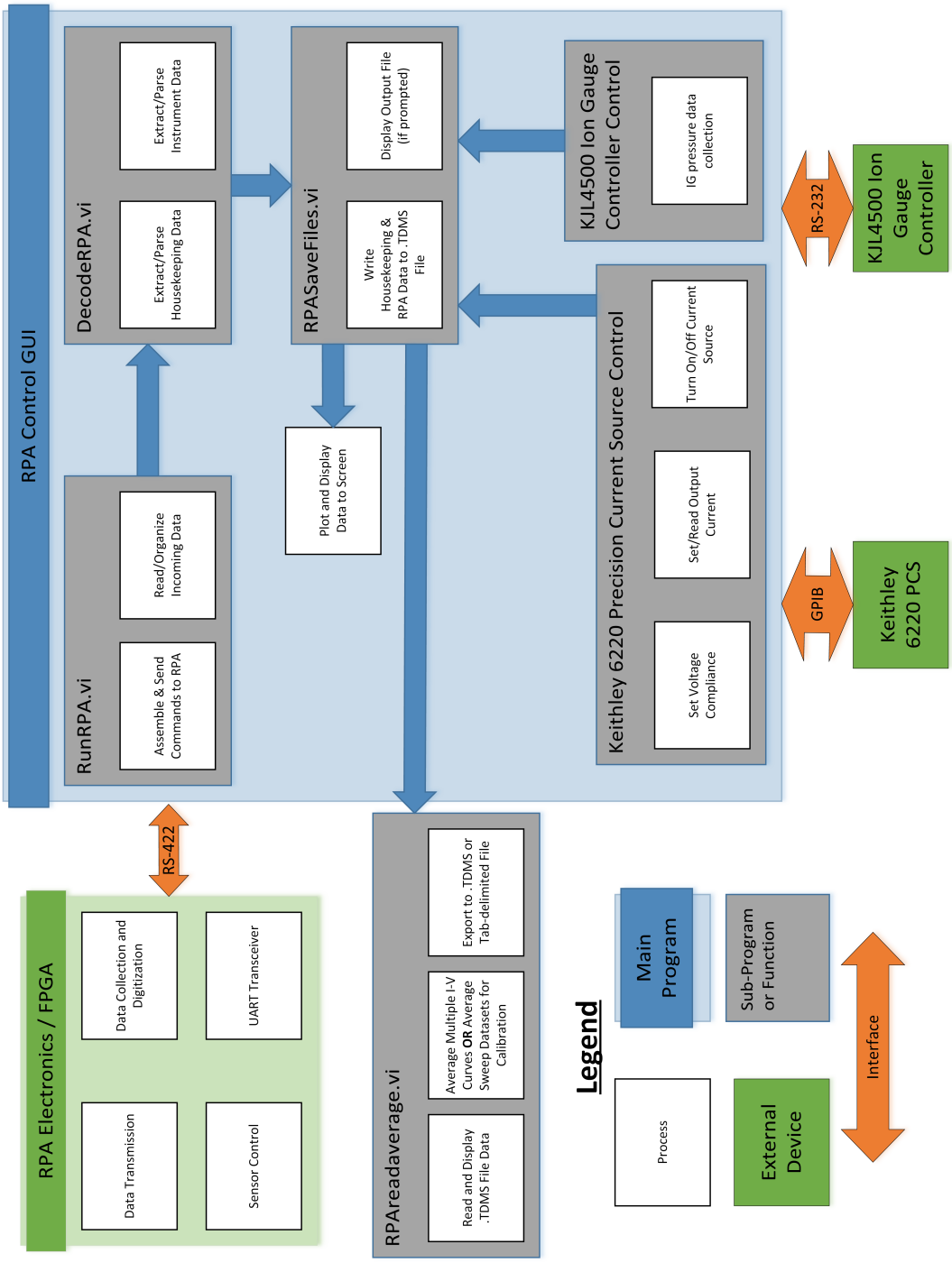

Figure 3.6: **RPA control code software block diagram.** The RPA control GUI uses various sub-programs to communicate with the RPA, apply engineering coefficients to the science and housekeeping data, and output the parsed data to a file and display on the front panel. The GUI console connects with and controls various external test support equipment as shown here.

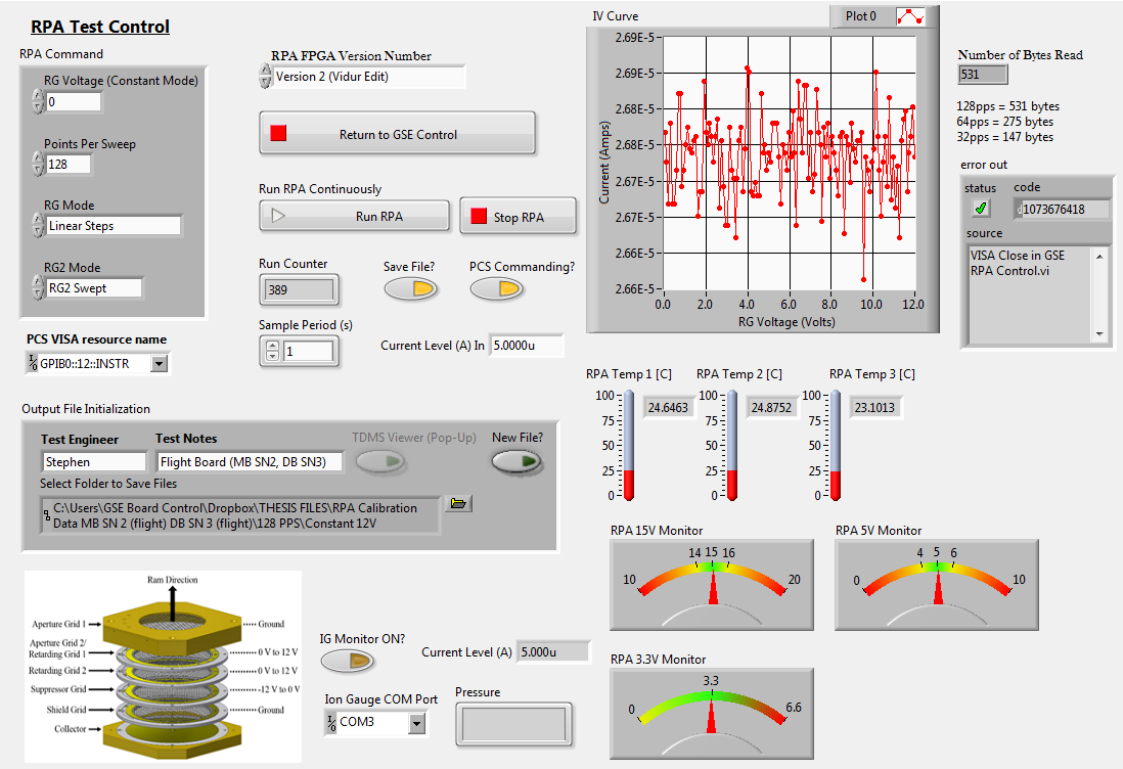

Figure 3.7: **RPA control VI front panel.** The RPA control code's GUI displays all of the housekeeping monitors as indicators, plots the RPA data, and allows the user to setup the data acquisition with drop-down menus and buttons. All controls can be accessed on the left side of the GUI window, while the right side of the window is reserved for indicators and monitors.

command control (in conjunction with an underlying section of code) disallows any invalid command. The "RG Voltage" command gets ignored by the program during any other mode than "Constant RG Voltage" mode since this uplink byte is shared with the "Step Size" command which is hard-coded for 32, 64, and 128 Points Per Sweep (PPS) in linear and smart sweep modes. The step size constants are the 16-bit representations of the numbers 2048, 1024, and 512 for 32, 64, and 128 PPS, respectively. This sets an equal spacing over the full 0-12 V sweep for each PPS mode.

The user has the ability to continuously command the RPA at cadences of one second or greater. This is crucial to performing efficient testing, and for monitoring changes in the ion characteristics. Figure 3.9 displays the main controls on the front panel of the LAICE RPA GUI.

After the command words get arranged, the GUI immediately opens a VISA (Virtual Instrument Software Architecture) interface to send the binary commands and then collect the incoming RPA data. The RPA outputs a variable-length data packet corresponding to each

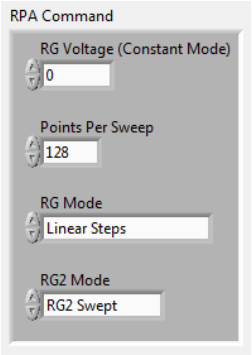

Figure 3.8: **LAICE RPA control GUI's RPA mode control.** The RPA Command LabView controls allow the user to easily select the wanted RPA mode via drop-down menus for each option. The command control in conjunction with a section of code in the editor disallows any invalid command.

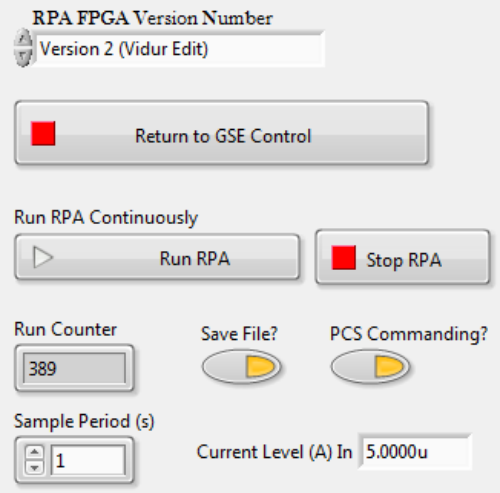

Figure 3.9: **LAICE RPA control GUI user controls.** Buttons on the GUI front panel allow the user to easily run and stop the RPA, start saving the incoming data, select the sample period, and see the current run count. An enable button and a current control for the Keithley 6220 Precision Current Source (PCS) is also included for use during calibration. The "Return to GSE Control" button allow the user to exit the GUI program.

points per sweep mode, so the software handles this automatically. Sub-routines are then called to parse this binary data into voltage signals and apply engineering coefficients to the housekeeping and science data. Raw data, the command modes, user-readable data, and test information are stored in a unique .TDMS file for each individual RPA sweep. Afterwards, the GUI displays the user-readable data on the front panel. Separate GUI's are used to read and combine data sets from multiple RPA sweeps. Appendix A discusses each GUI and subVI (Virtual Instrument function) in detail.

3.2 RPA Calibration

Since the LAICE RPA sends binary data via RS-422 serial protocol, the GUI must read and interpret the current samples by applying a set of calibration coefficients to the incoming 0 to 5 V readings to convert them into user-interpretable data. Prior to the testing listed in this document, the RPA relied on a theoretically-generated transfer function to convert the current sample data from 16-bit word counts into user-readable values. This resulted in errors across the entire input current range because of the uncertainties of the theoretical transfer function. To mitigate this uncertainty, the RPA electronics must be calibrated with accurately measured input currents.

A diagram of this RPA calibration test setup can be seen in Figure 3.10. A small current generated by a Keithley 6220 Precision Current Source tied to the RPA collector serves as the calibration current. The Keithley 6220 can source currents as low as 100 fA with nominal accuracy of less than 0.4% depending on the range mode, which is sufficient for the LAICE RPA calibration. Because of the voltage bias sensitivity of the LOG114 electrometer, the voltage compliance setting on the Keithley 6220 was set to 0.5 V as specified by the LOG114 data sheet. As the RPA performs a sweep, the collector will see the current provided by the Keithley 6220, and this current is read by the LOG114 electrometer. Since the sensor grids in front of the collector plate do not affect the constant current input in this setup, each sample within the sweep data corresponds to a reading of the same input current. This allows the user to collect 32, 64, or 128 samples per second depending on the selected mode, which can then be averaged together for calibration with the input current. After setting the current input level on the Keithley 6220, 3 to 5 sweeps were performed in each operational RPA mode and the results were averaged together and exported. The GUI then reads and saves the input current from the Keithley 6220 (via GPIB port) for comparison. The input current values of 100 pA to 10 μA were chosen such that the generated currents would span the full expected range of the LOG114 electrometer.

3.2.1 Keithley 6220 Precision Current Source (PCS)

Before performing a calibration, all support equipment was spot-checked to ensure the devices are within specification. In this case the most critical piece of support equipment is the Keithley 6220 Precision Current Source (PCS). The 6220 has a varying accuracy depending on the range mode in which the user operates the device. Table 3.1 shows the Keithley 6220 Precision Current Source accuracy level for each range setting.

In order to verify and quantify the accuracy of the 6220 in each of these range modes, this check was performed with a Keithley 6517B Electrometer. Both devices were connected via Tri-ax cable and the 6220 current was varied along the current range needed for the calibration. Figure 3.12 shows a spot check of the Keithley 6220 Precision Current Source's calibration with a Keithley 6517B Electrometer.

At the low range for the RPA calibration (100 pA) the PCS current output is within 0.5%,

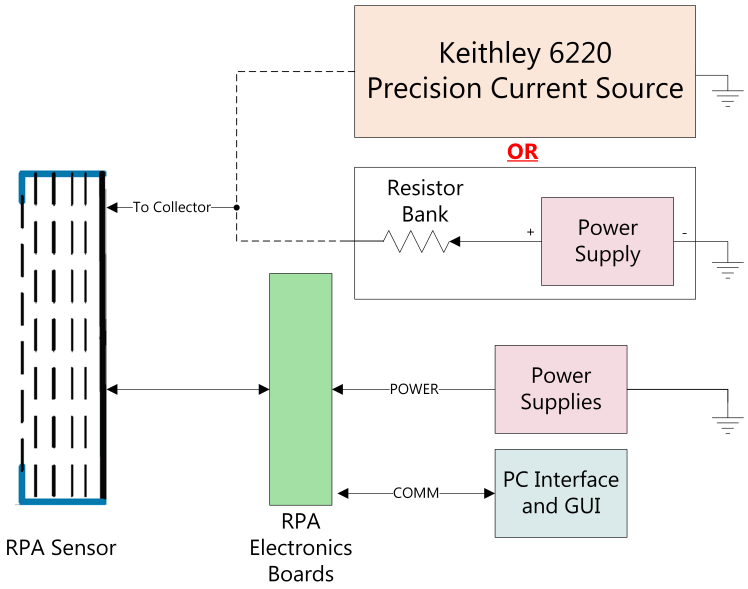

Figure 3.10: **RPA calibration test setup diagram.** The upper right section shows two methods used to provide a known input current to the RPA collector plate. Using the precision current source method yields more consistent input currents with less noise than the resistor-power supply method. When using the resister-power supply method, users should ensure the voltage on the collector end of the resistor does not exceed the 0.5 V maximum rating of the LOG114 electrometer. The precision current source method was used exclusively for all calibration curves generated in this paper.

Table 3.1: **Keithley 6220 Precision Current Source noise level by range setting.** This data are valid for 23C ±5C. (Keithley Instruments, Inc., 2008)

Range	**Accuracy ±(%rdg + amps)**	**Programming Resolution**
2 nA	0.4 % + 2 pA	100 fA
20 nA	0.3 % + 10 pA	1 pA
200 nA	0.3 % + 100 pA	10 pA
2 A	0.1 % + 1 nA	100 pA
20 A	0.05% + 10 nA	1 nA
200 A	0.05% + 100 nA	10 nA

while at the high end it is under 0.03%. When performing a calibration these relative accuracies should be noted, especially for input currents less than 100 pA.

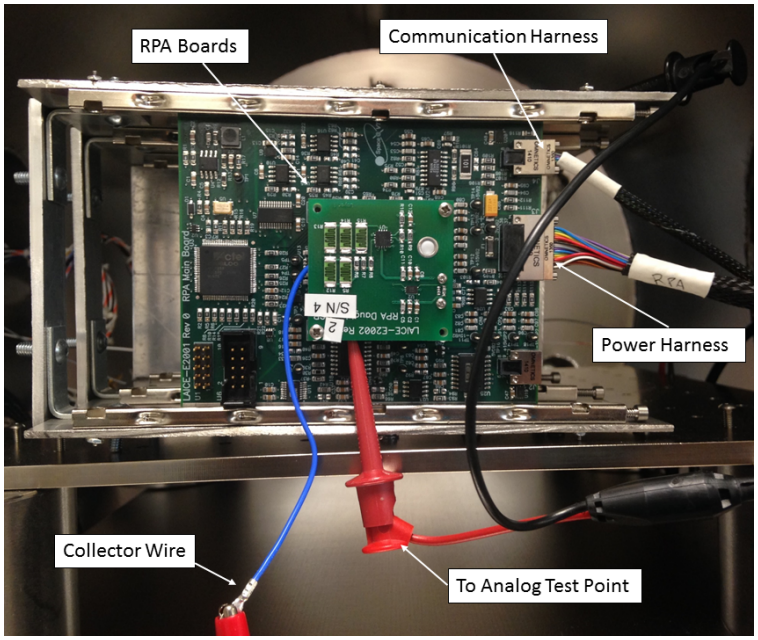

Figure 3.11: **Photograph of RPA calibration test setup in vacuum chamber.** Input current of 100 pA to 10 μA given to the collector wire using Keithley 6220 Precision Current Source. Analog signal test point 'TP6' was monitored during the calibration.

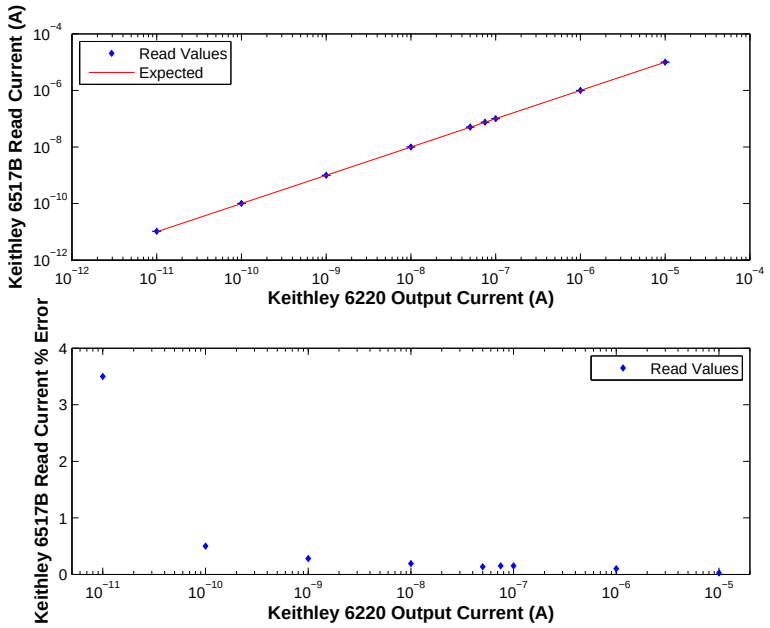

Figure 3.12: **Keithley 6220 Precision Current Source Calibration Spot Checks.** As expected the PCS is very accurate (<0.5%) for output currents over 100 pA.

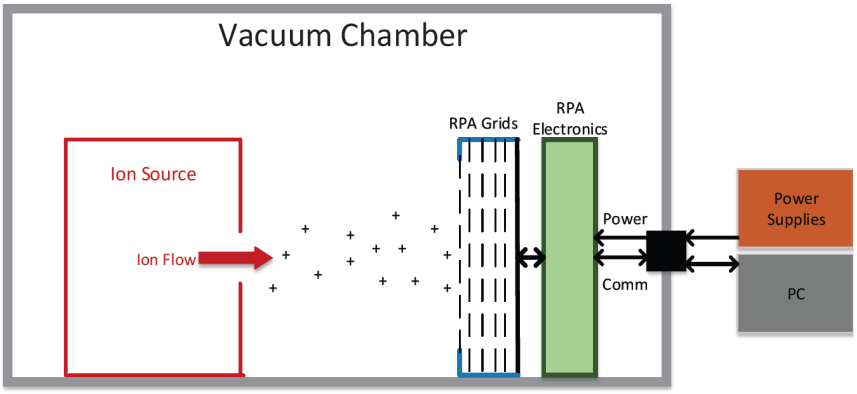

Figure 3.13: **LAICE RPA end-to-end test diagram.** The cable bundles for the power supplies and PC interface housed outside the vacuum chamber route through a feed-through in the chamber and to the RPA electronics box enclosure. The RPA electronics box houses the RPA electronics and shields the boards from stray electron impacts. The ion source propels a concentrated beam of ions toward the RPA aperture, generating a current on the collector plate. Lucy Fanelli. *Electronics for a versatile and robust retarding potential analyzer for use in nano-satellite platforms.* 2014. Masters thesis, Virginia Tech. Used under fair use, 2015.

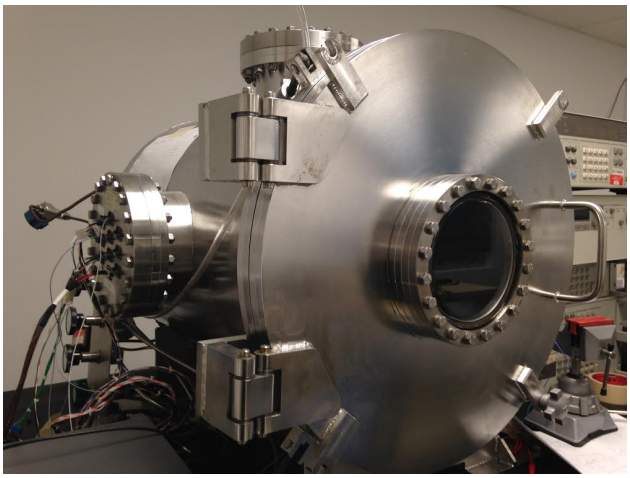

Figure 3.14: **Photograph of the Space@VT vacuum chamber.** Power and communication harnesses are connected through 9-pin D-subminiature feed-throughs.

3.3 RPA End-to-End Testing

The diagram of the end-to-end test setup in Figure 3.13 shows the configuration of the ion source and LAICE RPA in the vacuum chamber. The PC exterior to the chamber runs the RPA control GUI to analyze and save the data. End-to-end testing for the LAICE RPA was performed in a Space@VT vacuum chamber shown in Figure 3.14.

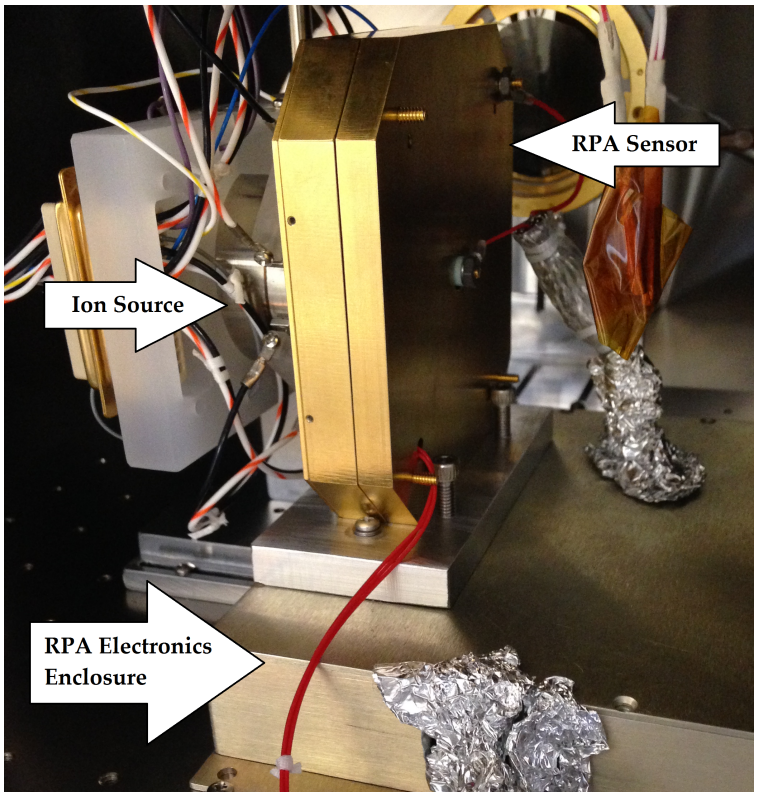

Figure 3.15: **Photograph of the LAICE RPA end-to-end test setup.** Aligning the apertures of the RPA sensor and ion source and adjusting the stand-off distance between them maximizes the current flowing into the RPA.

For the preliminary I-V curve testing, the ambient pressure in the vacuum chamber was reduced to approximately 1×10^{-7} Torr and then filled to 5×10^{-5} Torr with gaseous nitrogen. According to previous ion source testing (Dhar, 2013) this neutral pressure will allow the ion source to produce around 20 nA or more depending on its configuration. The ion source was placed about two inches in front of the RPA sensor aperture and centered with the aperture to allow for maximum ion beam collection in the RPA (Figure 3.15). A negatively biased grid (not shown) must be placed between the ion source and the RPA aperture so that energetic electrons do not reach the RPA aperture. Since the apertures of the RPA and source are at constant potentials this intermediate grid does not affect the energy of ions entering the RPA.

3.3.1 Ion Source

In order to validate that the LAICE RPA can accurately read ion currents in the LEO environment, end-to-end validation testing of the RPA sensor and electronics through to the GUI must be performed. Using the hot-filament ion source (Figure 3.16) developed at Virginia Tech, an ion beam is produced with densities and average energy comparable to what the LAICE spacecraft will encounter in the ionosphere.

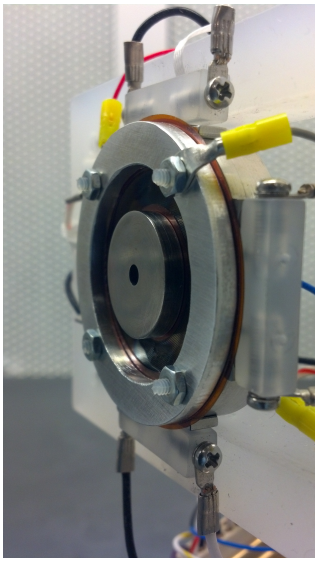

Figure 3.16: **Front view of the hot-filament ion source.** The hot-filament ion source built by Virginia Tech simulates the atmospheric plasma the RPA will move through on orbit. Carefully biased surfaces inside the ion source guide a beam of 100 eV electrons which collide with neutral gas leaked into the vacuum chamber to produce ions which are subsequently propelled toward the RPA. Photograph taken by Lee Kordella.

Table 3.2: **Ion source surface bias values.** The surfaces of the ion source were biased to these levels during end-to-end and sensitivity testing.

Surface	**Bias (V)**
Gutter	-95
Filament	-90
Repeller/Chamber	Varies (+21 to +50)
Grid	0
Electron Barrier	-120

Figure 3.17 shows a block diagram of the Virginia Tech hot-filament ion source. The ion source generates focused beams of electrons via coiled filaments which ionize neutral gas. Biased conductive surfaces route the electrons such that they ionize neutral gas in front of the repeller. The repeller surface propels the ions beyond the front plane of the ion source and towards the RPA, where the RPA sensor measures the incoming ion current. Figure 3.17 defines the five biased surfaces of the ion source configuration used in LAICE RPA end-to-end testing. The particular voltage level of each surface inside ion source can be found in Table 3.2.

The details of the inner workings of the ion source are beyond the scope of this paper but a reference to this deeper discussion can be found in Dhar 2013.

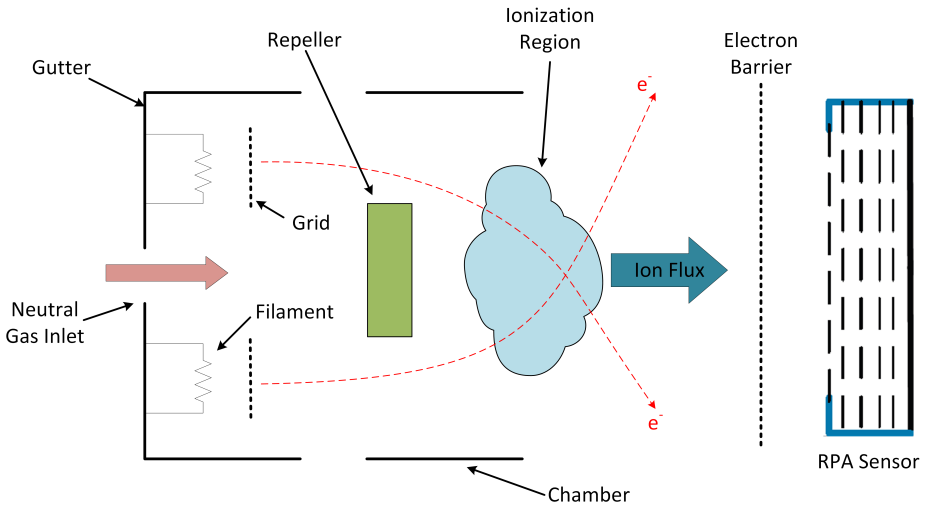

Figure 3.17: **Ion source block diagram.** The ion source generates focused beams of electrons via coiled filaments which ionize neutral gas. Specifically tuned biased surfaces route the electrons such that they ionize the neutral gas in front of the repeller. The positive voltage on the repeller surface propels the ions out of the ion source's aperture.

3.4 Chapter Summary

The RPA GUI functionality was designed to provide a user-friendly and robust interface for the LAICE RPA. This interface allows control over the full suite of RPA modes, the ability to save data easily and efficiently, and control over the critical external test support equipment. The setup and procedure for RPA calibration and RPA end-to-end testing (including sensitivity analysis) presented in this chapter provides a groundwork for the validation of not only this RPA, but also any future versions of this design. Chapter 4 presents the results from the testing described here in Chapter 3, as well as discussion of a fundamental electronics issue detected during calibration.

Chapter 4

Results and Discussion

4.1 ADC Conversion Issues

Early in the calibration process of the version 1 LAICE RPA electronics board, we detected an offset between the analog and digitized current signals. Using the version 1 RPA FPGA code described by Fanelli (2014), we provided a constant input current to the RPA electronics board and measured the analog signal voltage against the digital representation of that signal via the RPA control code GUI. When switching between 32, 64, and 128 PPS modes, the analog-to-digital offset increased as the number of points per sweep decreased. Originally, we suspected the offset may be due to an FPGA code error such as incorrect averaging. In the version 1 RPA FPGA code the oversampling value changes depending on which mode is operated. Another hypothesis was that the offset depended on the the number of oversamples taken. Table 4.1 defines the oversampling values for the version 1 FPGA code. The sampling wait time refers to the built-in delay between setting the RG voltage and initiating the signal line sampling.

To test this hypothesis, we created multiple versions of the FPGA code with consistent oversampling values between modes (oversampling ranging from 2 to 1024). We then conducted a study of the difference between the analog and digital current readings at two different input currents while using the same sweep mode (32 PPS, RG2 swept in this case). Other modes were spot-checked for consistency with the reading from this mode. The results of this study can be seen in Figure 4.1. The signal difference was more pronounced at the 5000

Table 4.1: **LAICE RPA FPGA version 1 code oversampling values.**

Mode	Oversampling	Sampling Wait Time (ms)	Sweep Time (ms)
32 PPS	1024	12	738
64 PPS	512	12	947
128 PPS	128	6	993

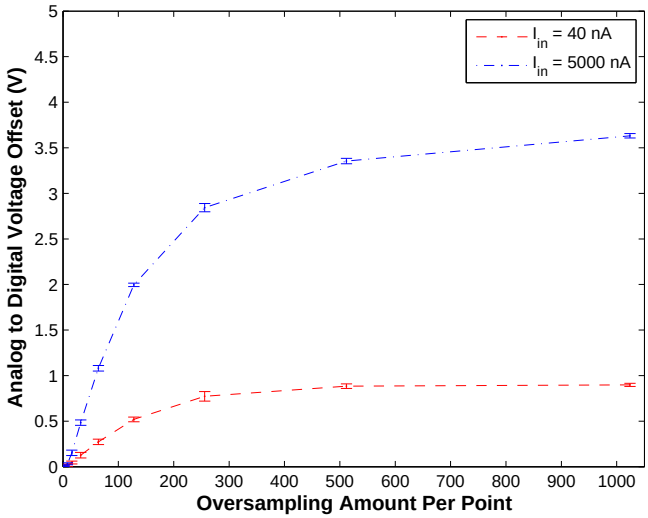

Figure 4.1: **Plot of analog and digital signal voltage difference vs. oversampling amount.** Input currents of 40 nA and 5000 nA were used in this trial. All samples were taken in 32 PPS mode with RG2 swept, using the version 1 RPA FPGA code.

nA input current and consistently worse at greater oversampling values.

The next step in the investigation included probing the analog current signal (test point "TP6" on the RPA Main Board schematic - see Appendix E) and the retarding grid voltage (test point "TP2"). Probing the RG voltage provides an indication of when the input current gets sampled in reference to the change of RG voltage. Figure 4.2 shows these values sampled with an oscilloscope for the 32 PPS, RG2 swept mode with an input current of 40 nA and an oversampling amount of 128. The spike on the analog current line is likely due to system noise induced by setting a new RG voltage, but the expanded shape of the analog signal prior to that spike was not expected. Figure 4.3 shows results from the same test performed with 256 instead of 128 oversampling. The expanded region of the spike becomes more pronounced, and Figure 4.4 similarly shows the even more elongated plateau at 512 oversampling.

Because the shape of the ramp-up in the spike's extended region looked suspiciously like the charging of a capacitor in an RC circuit, we suspected this offset might be caused by a problem with the ADC. By examining the ADC datasheet, we discovered a clause stating the input impedance of both the CHX (analog input channel) and the COM input (reference voltage) should match. This is not the case in the RPA circuit design. Additional information from the datasheet specified that this impedance mismatch could cause offsets between the inputs and output lines, but that reducing the ADC clock rate could mitigate the issue. We reduced the ADC clock rate from 2.5 MHz to 1.25 MHz and re-tested the 512 oversampling case. As seen in Figure 4.5 the plateau region visually disappeared in this case. The measured offset between the analog and digital signals became unnoticeable as well, with any offset

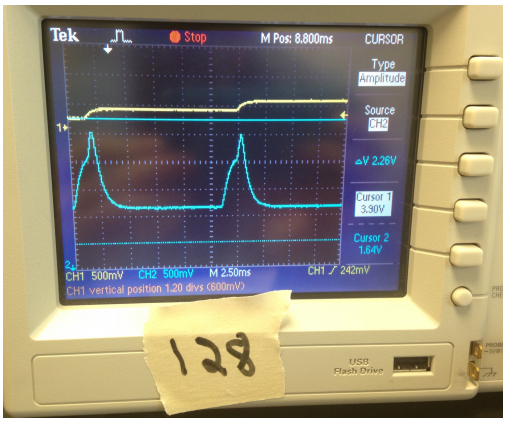

Figure 4.2: **Oscilloscope reading of the analog current signal (blue) and the Retarding Grid voltage (yellow) for 32 PPS and 128 oversampling points.** Input current of 40 nA was used in this trial. A noise spike was expected on the analog current line, but the expanded shape of the analog signal prior to the spike was not.

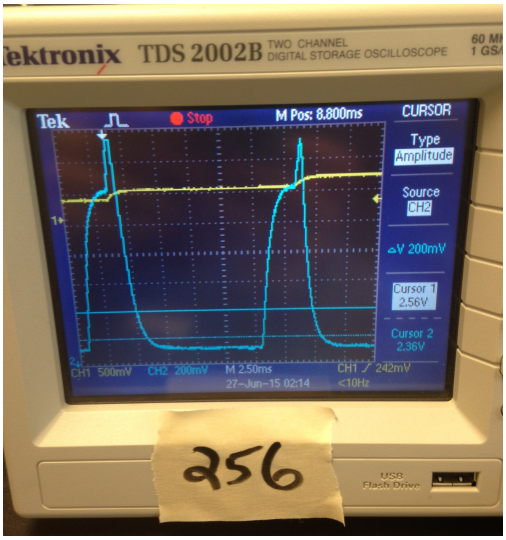

Figure 4.3: **Oscilloscope reading of the analog current signal (blue) and the Retarding Grid voltage (yellow) for 32 PPS and 256 oversampling points.** Input current of 40 nA was used in this trial. The "plateau" extended region of the analog signal becomes even more pronounced than in the case with less oversampling.

deltas falling within the noise level of the instrument.

By reducing the oversampling and instituting a longer fixed wait time after the RG voltage change, the ADC signal offset was reduced to the noise level of the RPA electronics, if not eliminated altogether. The original design of the LAICE RPA included generous oversampling amounts at each step of the sweep, and these FPGA code fixes greatly reduce those values,

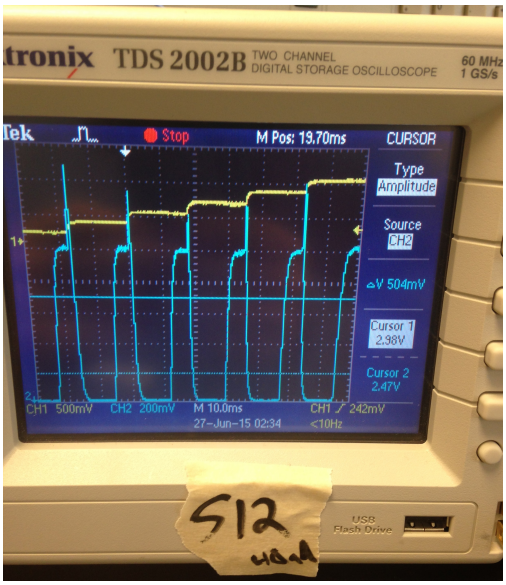

Figure 4.4: **Oscilloscope reading of the analog current signal (blue) and the Retarding Grid voltage (yellow) for 32 PPS and 512 oversampling points.** Input current of 40 nA was used in this trial. The "plateau" extended region of the analog signal becomes even more pronounced and elongated relative to the previous examples.

Figure 4.5: **Oscilloscope reading of the analog current signal (blue) and the Retarding Grid voltage (yellow) for 32 PPS and 512 oversampling points.** Input current of 10 μA used in this trial. The "plateau" extended region of the analog signal is not visually noticeable.

limiting the amount of averaging performed at each point. We don't expect the flight data to be affected considerably though, since the version 1 FPGA code instituted oversampling at the clock speed (2.5 MHz) and there are few on-orbit effects that would cause the signal to fluctuate at that frequency. The PIs will therefore utilize multi-sweep averaging of flight data to reduce the noise level, if needed.

Table 4.2: **LAICE RPA FPGA versions 1 and 2 oversampling and clock rate specification comparison.** Multiple changes to the original RPA FPGA code were made prior to final calibration. The list of changes and effects of those edits to the code are detailed in this table.

Specification	Original FPGA Code	Final FPGA Code
ADC Clock Rate	2.5 MHz	1.25 MHz
32 PPS sweep time	738 ms	840 ms
64 PPS sweep time	947 ms	830 ms
128 PPS sweep time	993 ms	820 ms
32 PPS oversampling	1024 samples	2 samples
64 PPS oversampling	512 samples	2 samples
128 PPS oversampling	128 samples	2 samples
32 PPS wait time	12 ms	26 ms
64 PPS wait time	12 ms	13 ms
128 PPS wait time	6 ms	6.35 ms
32 PPS signal offset at 40 nA	1.04 V	0.02 V
64 PPS signal offset at 40 nA	0.92 V	0.02 V
128 PPS signal offset at 40 nA	0.67 V	0.02 V

The wait time for each mode was increased in order to allow more time for the current signal to stabilize. The previous FPGA code's wait time for the 128 PPS was less than 1 ms longer than the observed 5 ms approximate settling time on the ADC input line. Another beneficial change was to match the the total sweep times of each PPS mode as close as possible to a constant value. This constrains each sweep mode to a consistent spatial resolution on-orbit and will allow sweeps taken in different modes to be compared more easily (since the effective plasma volume the sensor passes through on-orbit will be constant). Table 4.2 compares the values of the oversampling in each mode, and the ADC clocking rate, to the final FPGA code values, and shows the offset between the analog and digitized currents in each case.

In future versions of this RPA circuit care must be taken to match the impedance between the analog inputs and the reference line, and the clock rate should be minimized to prevent this issue from recurring.

4.2 RPA Calibration Results

The calibration curves for the LAICE RPA instrument electronics can be seen in Figure 4.6, 4.7, and 4.8. The logarithmic curve fit generated from these data were used in the RPA data parsing code to assign engineering values to the collector current readings. This test was performed at atmosphere and inside the Space@VT vacuum chamber to limit EMI effects. Each point on a calibration curve is the mean of at least 96 samples, and in some cases as many as 600. The error bars represent the standard deviation from the mean of each calibration point. For each of the 32, 64, and 128 PPS calibrations data were collected over

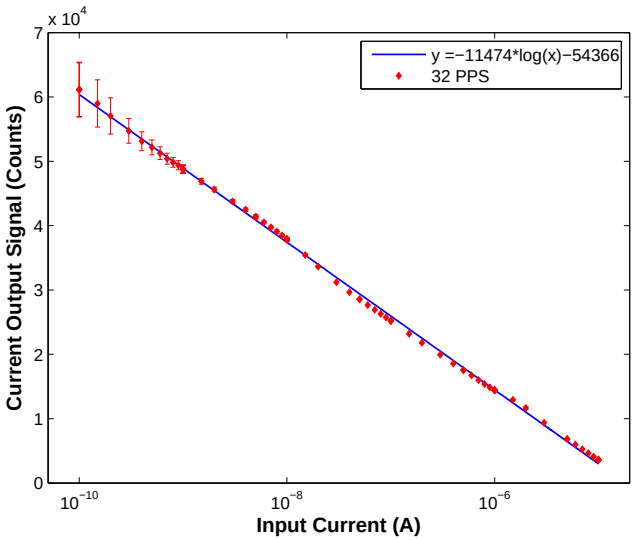

Figure 4.6: **LAICE RPA 32 PPS calibration curve.** The calibration was performed over collector current input ranges of 100 pA to 10 μA. Output digital current signals were read at the LabView console. The test was performed at atmosphere, room temperature, and inside the Space@VT vacuum chamber to limit EMI.

the entire input current range in each of the RPA sub-modes (linear sweep, smart sweep, and constant RG1 voltage) as well as the additional mode properties (RG2 swept or grounded and the constant RG1 voltage using 0 V, 6 V, and 12 V). This provides a comprehensive comparison of the data collected in each sub-mode in order to identify any discrepancies between them.

Error in the calibration data can be attributed to noise level limitations, especially near the lower current limits of the Keithley 6220. The coefficients from this curve fit were fed back into the parsing code to convert the incoming raw collector current data into user-readable currents in nanoamps.

Table 4.3 summarizes the fit results from the 32, 64, and 128 PPS calibrations. The curve fits for each PPS mode are very consistent, validating that the choice of PPS mode no longer causes the input current to output signal transfer function to change (as it did in the version 1 FPGA code).

4.3 RPA Noise Analysis Results

Figure 4.9 displays the results from the LAICE RPA noise testing of the 32 PPS mode. This study covered a span of multiple runs of the LAICE RPA with various currents applied to the collector wire. The deviation from the expected value on the y-axis provides average values at each input current provided by the Keithley 6220 Precision Current Source. This test was performed at atmosphere and inside the Space@VT vacuum chamber to limit EMI.

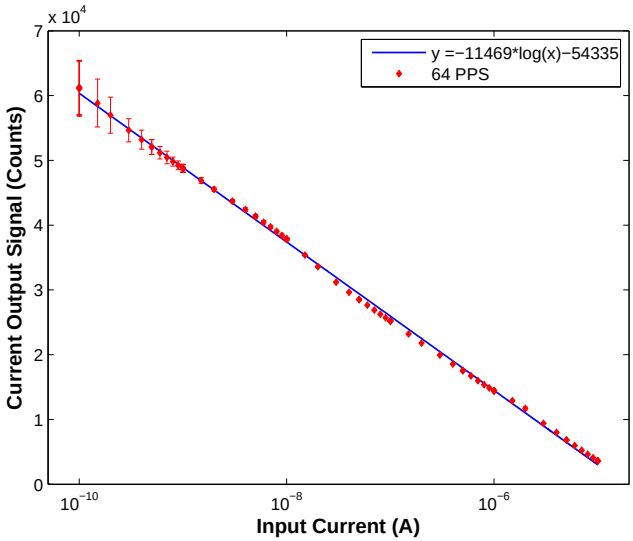

Figure 4.7: **LAICE RPA 64 PPS calibration curve.** The calibration was performed over collector current input ranges of 100 pA to 10 μA. Output digital current signals were read at the LabView console. The test was performed at atmosphere, room temperature, and inside the Space@VT vacuum chamber to limit EMI.

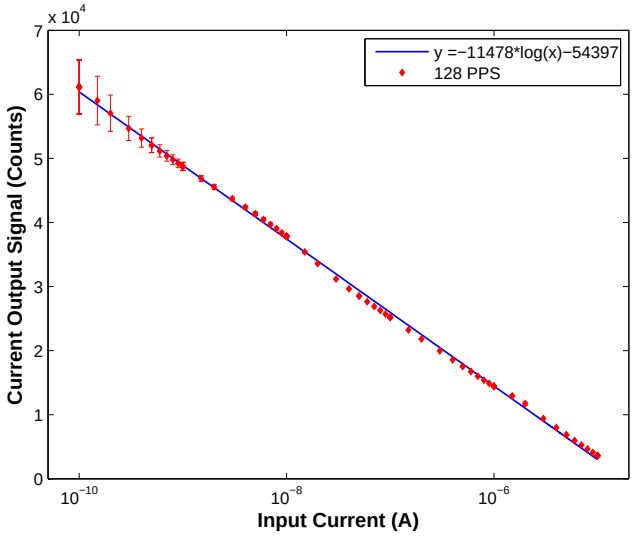

Figure 4.8: **LAICE RPA 128 PPS calibration curve.** The calibration was performed over collector current input ranges of 100 pA to 10 μA. Output digital current signals were read at the LabView console. The test was performed at atmosphere, room temperature, and inside the Space@VT vacuum chamber to limit EMI.

Table 4.3: **RPA mode calibration curve fit coefficients.** All coefficients correspond to the equation $y = a \times log_{10}(x) + b$ where "x" is the input current in Amps and "y" is the RPA output signal in a decimal-represented 16-bit count.

Mode	a (Counts)	b (Counts)	R^2
32 PPS	-11474	-54366	0.9991
64 PPS	-11469	-54335	0.9991
128 PPS	-11478	-54397	0.9992

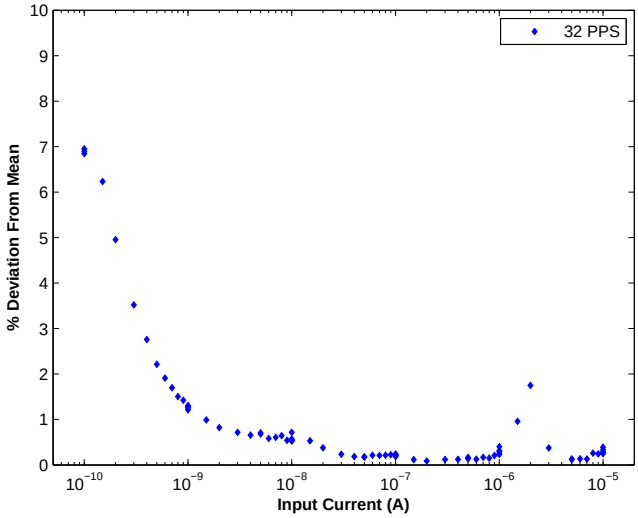

Figure 4.9: **LAICE RPA electronics noise analysis for 32 PPS.** The input current along the entire RPA specified range (100 pA to 10 μA) was tested for each 32 PPS sub-mode. The percent deviation from the mean for each calibration point is plotted on the independent axis. As expected, current measurements close to the low-end range of the RPA electrometer have more noise on the reading compared to the high-end range.

In practice the LAICE RPA is also limited by the LOG114 electrometer's input current suggested low range of 100 pA and the relative error depending on which Keithley 6220 input range is selected. Results from similar studies in the 64 and 128 PPS modes can be found in Figure 4.10 and Figure 4.11, respectively. As with the calibration curves for each mode, the relative noise across the input current range is consistent over each PPS mode.

In order to visualize the goodness-of-fit for the calibration, residuals plots were generated along with a percent error from fit plot to show consistently how the curve fit applies to the entire input current range. Figures 4.12, 4.13, and 4.14 contain this data. The 32, 64, and 128 PPS residuals plots all display a very similar structure, further indicating the consistency between each mode's calibration. The residuals for each case across the input current range vary above and below the best fit line in a relatively systematic way. The PPS mode residuals

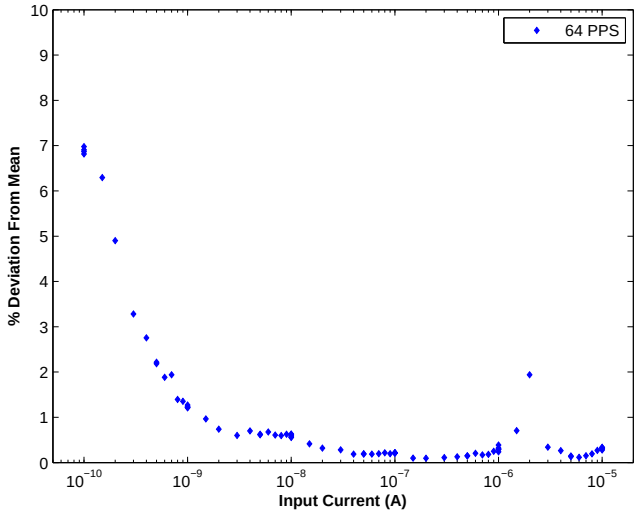

Figure 4.10: **LAICE RPA electronics noise analysis for 64 PPS.** The input current along the entire RPA specified range (100 pA to 10 μA) was tested for each 64 PPS sub-mode. The percent deviation from the mean for each calibration point is plotted on the independent axis. As expected, current measurements close to the low-end range of the RPA electrometer have more noise on the reading compared to the high-end range.

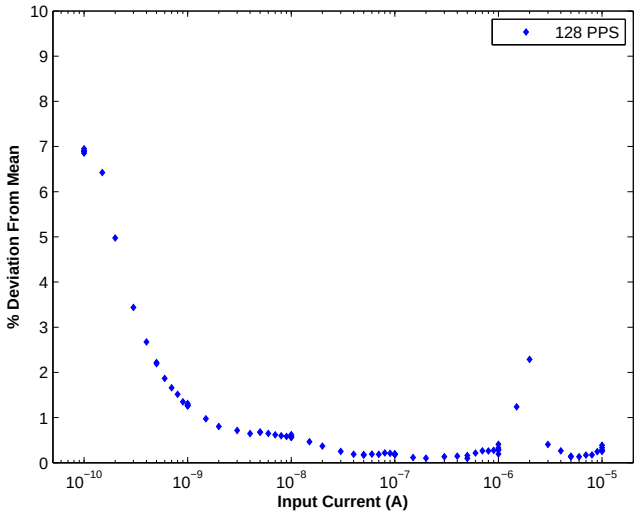

Figure 4.11: **LAICE RPA electronics noise analysis for 128 PPS.** The input current along the entire RPA specified range (100 pA to 10 μA) was tested for each 128 PPS sub-mode. The percent deviation from the mean for each calibration point is plotted on the independent axis. As expected, current measurements close to the low-end range of the RPA electrometer have more noise on the reading compared to the high-end range.

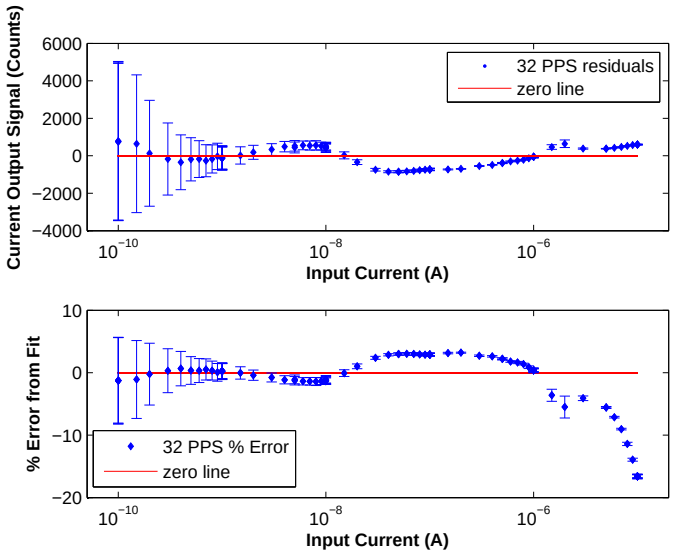

Figure 4.12: **LAICE RPA electronics best fit line analysis for 32 PPS.** The top subplot shows the residual analysis for the 32 PPS calibration and best fit line. The error bars again reference the standard deviation from the mean for that particular calibration point. The bottom subplot shows the percent error comparison of the measured calibration point to the best fit line.

plots across the PPS modes are at least encouraging from a consistency standpoint. The percent error from fit plots show the relative error of each calibration point from the best fit line's expected value. This plot helps to evaluate how well the best-fit line predicts each individual current reading across the range. The low-end input currents around 100 pA are all predicted within 2%, while the best fit line's error increases considerably to almost 20% near 10 μA. At this regime of the calibration range, small offsets in the best fit prediction and the measured current value can lead to increased percent error.

4.4 RPA End-to-End Testing Results

Figure 4.15 displays an averaged I-V characteristic performed in vacuum over five consecutive sweeps with the 32 PPS, linear, RG2 Swept mode. The I-V characteristic's regression of collector current along the sweep voltage indicates the RPA sensor successfully repels the ions generated by the ion source in this test. This full end-to-end check from a simulated plasma environment, through the RPA sensor, read and digitized by the RPA electronics, and finally parsed and displayed by an external device confirms the functionality of the LAICE RPA sub-system.

In order to validate the functionality of the LAICE RPA over the expected on-orbit pressure range, a test of instrument pressure sensitivity was performed in the Space@VT vacuum chamber. For this test, the 128 PPS ion trap mode (each retarding grid held to 0 V) was selected. Averaging the entire 128-point sweep together over at least eight seconds establishes

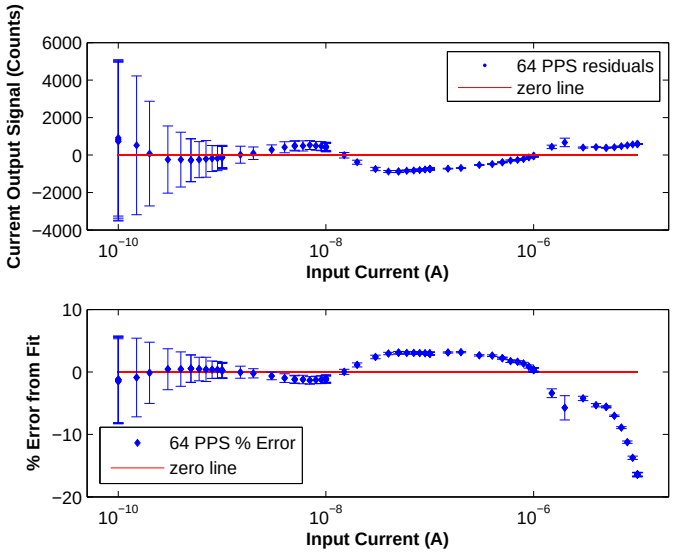

Figure 4.13: **LAICE RPA electronics best fit line analysis for 64 PPS.** The top subplot shows the residual analysis for the 64 PPS calibration and best fit line. The error bars again reference the standard deviation from the mean for that particular calibration point. The bottom subplot shows the percent error comparison of the measured calibration point to the best fit line.

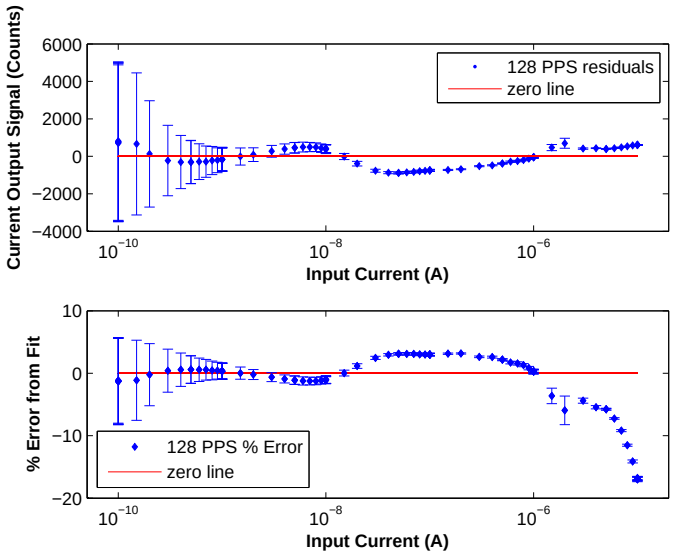

Figure 4.14: **LAICE RPA electronics best fit line analysis for 128 PPS.** The top subplot shows the residual analysis for the 128 PPS calibration and best fit line. The error bars again reference the standard deviation from the mean for that particular calibration point. The bottom subplot shows the percent error comparison of the measured calibration point to the best fit line.

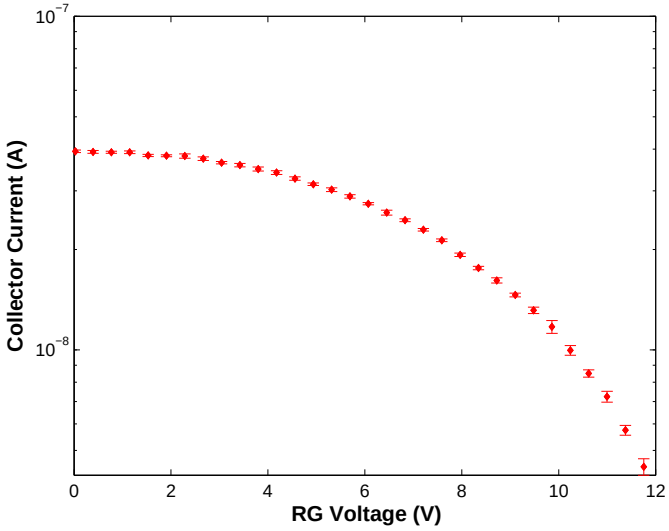

Figure 4.15: **Averaged RPA I-V Curve.** I-V characteristic averaged over five seconds (five sweeps), with the chamber pressure at 20 μTorr and the ion source repeller voltage of 32 V.

the ion current value without any retarding grid obstruction to the read current. If the LAICE RPA is truly capable of measuring ion current, one should see a relatively linear increase in the collector current as the chamber pressure increases. Figure 4.16 shows exactly this trend, thus validating the LAICE RPA's ability to measure variations in ion current across various pressures.

The results of the energy sensitivity analysis can be found in Figure 4.17. The repeller voltage inside the ion source was varied from 22 - 32 V in 2 V increments to cause changes in the average velocity of ions existing the source, and the results measured from the RPA were averaged over at least five sweeps to establish accurate error bars. The goal of this test was to demonstrate that the RPA is sensitive to the velocity distribution of the ionized gas. The mean energy of the ion beam can be controlled in part by varying the ion source repeller surface bias. As the repeller voltage increases the mean energy increases with the ion velocity. When this is done, one should see an overall increase in ion current across the sweep as well as movement of the "knee" in the curve to higher retarding voltages. Figure 4.17 shows exactly this expected dependency on ion beam speed, thus validating the LAICE RPA subsystem operation across varying beam speeds and energy ranges.

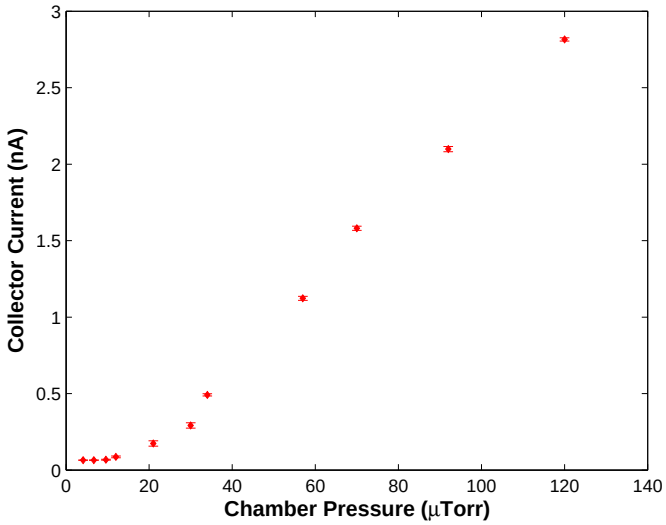

Figure 4.16: **RPA neutral pressure sensitivity analysis plot.** Plot generated by increasing the vacuum chamber pressure incrementally and taking "ion trap" measurements (constant stepping mode, RG voltage of 0 V). This configuration allows the RPA to collect all of the incoming ions due to the disabled RG. Chamber pressure read by a Varian 0571-K2471-304304 ionization gauge sampled with a Lesker KJL 4500 ion gauge controller.

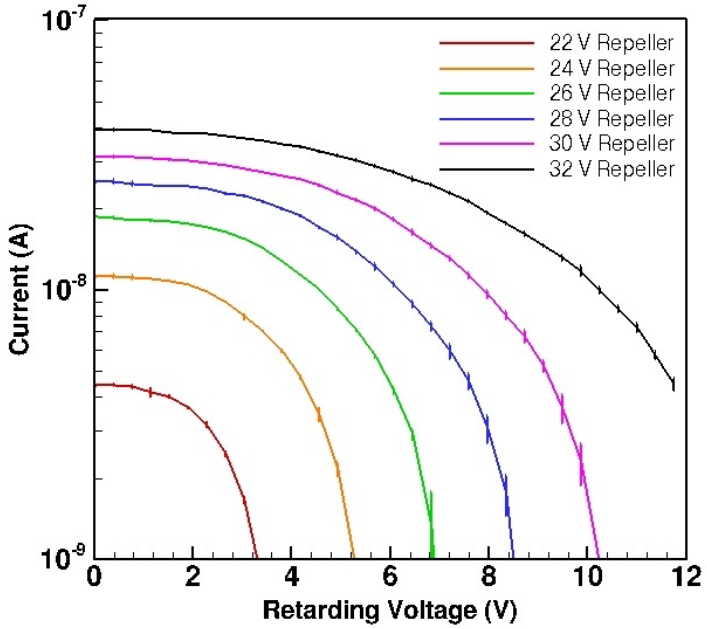

Figure 4.17: **RPA ion energy sensitivity analysis plot.** Plot generated by incrementally increasing the repeller surface bias inside the source and averaging the resulting I-V curves. Data taken in 32 PPS mode with the RG2 swept mode enabled. Chamber pressure set to constant 20 μ Torr with gaseous nitrogen.

Chapter 5

Conclusions and Future Work

5.1 Summary of Results

While Fanelli (2014) concentrated on the electrical and software design of the LAICE RPA, this paper presents a comprehensive calibration using specifically-designed LabView GUIs to prepare the LAICE RPA for flight. We validated the LAICE RPA functionality by subjecting the sub-system to energy sensitivity, pressure sensitivity, and noise estimation studies. Identifying and solving the observed problem with digitized current offsets has greatly improved the reliability and accuracy of this RPA. User interface tools, instrument drivers, and procedures listed here will help expedite future RPA calibration processes and provide a framework for users to adapt additional software or hardware changes as needed.

5.2 Future Work

The next steps in fully qualifying the LAICE RPA for flight include calibration and housekeeping spot checks over flight temperature ranges, LAICE VT payload sub-system integration and EMI testing, and vibration testing. Much of this testing will be performed on a spacecraft level after integration of the payloads.

Temperature range calibration - Functionality tests will also be performed while the RPA undergoes thermal environmental testing to determine how the calibration holds at extreme temperatures the instrument will be exposed to on-orbit. The calibration procedure described here should at least be repeated while the RPA sensor and electronics are held at approximately -20 °C and +85 °C in order to catalog any variance in RPA operation at the temperature extremes.

LAICE VT payload sub-system integration and EMI testing - The calibration and nominal performance data listed in this paper should be spot-checked after VT payload system integration. Any noise or signal level offsets should be recorded, and - if severe enough - additional measures should be taken to identify the source of the EMI and mitigate

or calibrate the response.

Vibration testing - Neither the LAICE RPA sensor nor the electronics have undergone comprehensive shock and vibration testing. Once assigned a launch provider, the RPA subsystem will be subjected to launch provider vibration specifications as part of the satellite integration. Afterwards, the team will conduct functionality spot checks of the RPA, including testing each grid of the RPA sensor while sweeping, and checking the throughput of input current to digitized data. A precision current source will be used to ensure all harnesses and connections are secured and operating correctly.

Bibliography

Davidson, R. L. and G. D. Earle (2011, January). A design approach for improving the performance of single-grid planar retarding potential analyzers. *Physics of Plasmas 18*(1), 012905.

Dhar, S. (2013). Ionospheric simulator (ionsim): Simulating ionospheric conditions in a vacuum chamber. Master's thesis, Virginia Tech.

Fanelli, L. (2014). Electronics for a versatile and robust retarding potential analyzer for use in nano-satellite platforms. Master's thesis, Virginia Tech.

Fanelli, L., S. Noel, et al. (2016). A versatile retarding potential analyzer for nano-satellite platforms. *Review of Scientific Instruments*. Manuscript submitted for publication.

Hanson, W. B. et al. (1981, December). The Retarding Potential Analyzer for Dynamics Explorer-B. *Space Science Instrumentation 5*, 503–510.

Keithley Instruments, Inc. (2008). *Keithley Model 6220 DC Current Source Model 6221 AC and DC Current Source* (C ed.). Keithley Instruments, Inc.

Kil, H. and R. A. Heelis (1998, January). Global distribution of density irregularities in the equatorial ionosphere. *Journal of Geophysical Research 103*, 407–418.

Klenzing, J. H., G. D. Earle, and R. A. Heelis (2008, June). Errors in ram velocity and temperature measurements inferred from satellite-borne retarding potential analyzers. *Physics of Plasmas 15*(6), 062905.

Knudsen, W. C. (1966, October). Evaluation and demonstration of the use of retarding potential analyzers for measuring several ionospheric quantities. *Journal of Geophysical Research 71*, 4669–4678.

Westerhoff, J. et al. (2015). Laice cubesat mission for gravity wave studies. *Advances in Space Research* (ASR-D-14-00786R1).

Zuccaro, D. R. and B. J. Holt (1982, October). A technique for establishing a reference potential on satellites in planetary ionospheres. *Journal of Geophysical Research 87*, 8327–8329.

Appendix A

LabView Code Discussion

A.1 RunRPA.vi

"RunRPA.vi" is a sub-VI for the "RPAcontrol.vi" user interface code which takes inputs of VISA (Virtual Instrument Software Architecture) interface reference, RPA command cluster, and error cluster and returns the RPA data in a byte array, and the total number of bytes read. The sub-VI icon inputs and outputs can be seen in A.1. Inputs are shown on the left side of the program icon while outputs are on the right side.

Figure A.2, Figure A.3, and Figure A.4 show the conditional structures connected to the "PPS Mode" control and contained in the VI block diagram of the code.

Figure A.5, Figure A.6, and Figure A.7 show the conditional statements that initialize the uplink commands to the RPA for the "Constant," "Linear Sweep," and "Smart Sweep" modes.

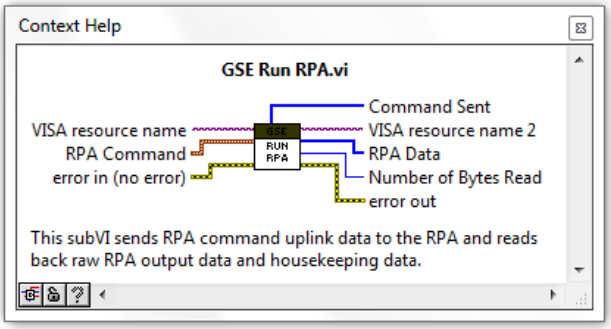

Figure A.1: **RunRPA subVI inputs and outputs definition.** The Run RPA VI takes inputs of VISA interface reference, RPA command cluster, and error cluster and returns unique outputs of the RPA data in a byte array and the number of bytes read by the PC. Required inputs displayed in boldface.

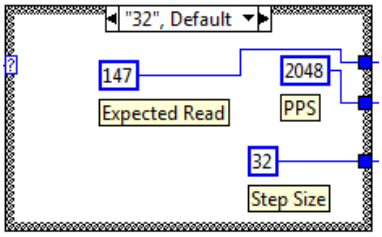

Figure A.2: **Conditional statement in "RunRPA.vi" for 32 PPS mode.** The constants inside the conditional statement get routed to the "expected bytes read" check, the "PPS mode" control, and the "PPS step size" control.

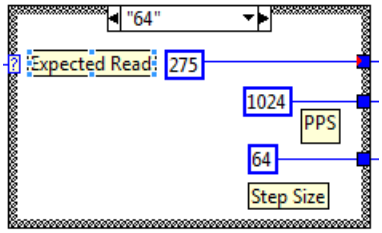

Figure A.3: **Conditional statement in "RunRPA.vi" for 64 PPS mode.** The constants inside the conditional statement get routed to the "expected bytes read" check, the "PPS mode" control, and the "PPS step size" control.

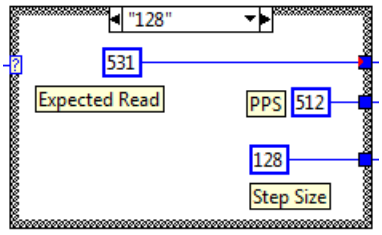

Figure A.4: **Conditional statement in "RunRPA.vi" for 128 PPS mode.** The constants inside the conditional statement get routed to the "expected bytes read" check, the "PPS mode" control, and the "PPS step size" control.

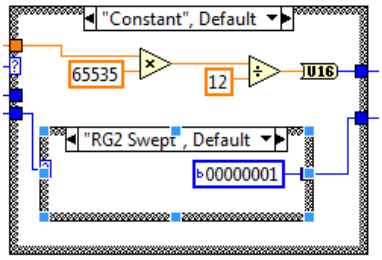

Figure A.5: **RPA mode conditional structure for Constant RV mode.** The code initializes the RPA command byte for "Sweep Mode" and converts the user-readable constant voltage value and converts it into a 16-bit word count.

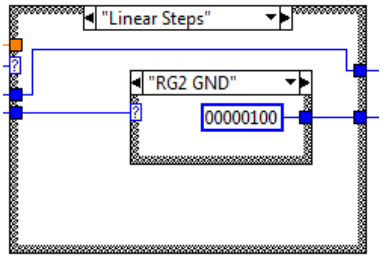

Figure A.6: **RPA mode conditional structure for Linear Sweep mode.**

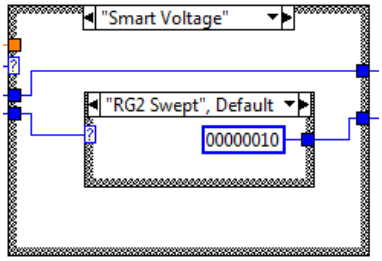

Figure A.7: **RPA mode conditional structure for Smart Sweep mode.**

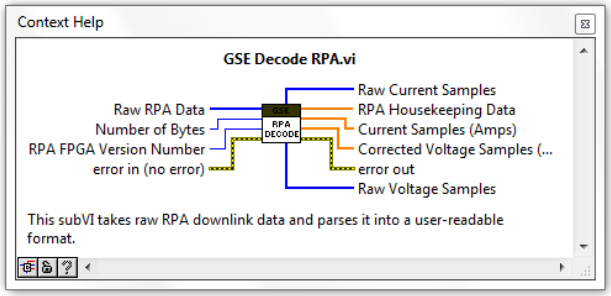

Figure A.8: **Decode RPA subVI inputs and outputs definition.** The Decode RPA VI takes inputs of RPA data in a byte array, the number of bytes read by the PC, the FPGA code version reference number, and error cluster and returns unique outputs of raw current samples in counts, an array of housekeeping data in engineering units, an array of current samples in amps, an array of RG voltage samples in volts, the output error cluster, and raw voltage samples in counts. Required inputs in boldface.

A.2 DecodeRPA.vi

The "DecodeRPA.vi" sub-VI takes the outputs of "RunRPA.vi" including LAICE RPA output data organized in a byte array, the number of bytes read by the GUI, the FPGA code version reference number, and error cluster and returns unique outputs of raw current samples in counts, an array of housekeeping data in engineering units, an array of current samples in amps, an array of RG voltage samples in volts, the output error cluster, and raw voltage samples in counts. This sub-VI extracts the signal voltages from the incoming raw 16-bit word counts incoming, applies transfer functions to the housekeeping and science data, and outputs the data to then be displayed by the GUI and saved into an output file by "RPAsavefiles.vi."

A.3 RPAsavefiles.vi

The sub-VI "RPAsavefiles.vi" takes various inputs of raw and parsed data as well as the sent command, vacuum chamber pressure, and the location of the output file and generates an MS Excel-readable .TDMS file containing the various inputs and other information about the last RPA sweep. Ease of data extraction within LabView and MS Excel along with user-defined and easily editable headers are the main benefits to using .TMDS files over .CSV or similar formats. A .TMDS file can be easily converted to a .CSV with LabView or MS Excel if the user desires. Additionally, .TDMS files have the ability to host multiple sheets of data, further organizing the output file. In the case of "RPAsavefiles.vi," the test information, housekeeping data, instrument data, and raw output data get stored on separate sheets for this reason. Figure A.9 displays the inputs and outputs of the "RPAsavefiles.vi" code. Figure A.10 shows the built-in sub-VIs used in the creation of "RPAsavefiles.vi." These built-in subVIs are used to create, modify, and input data into the .TDMS file structure. Figure A.11

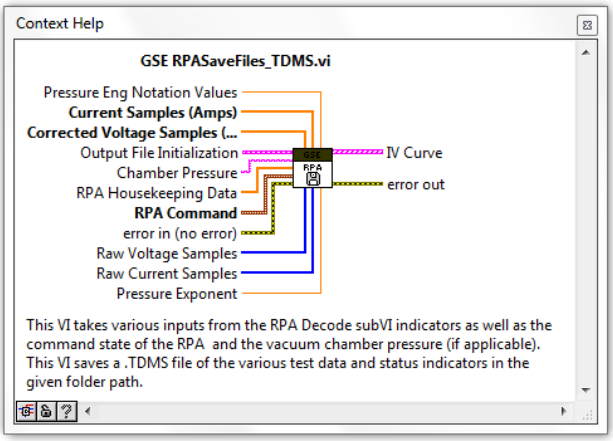

Figure A.9: **RPA Save Files subVI inputs and outputs definition.** The RPA Save Files VI takes various inputs of raw and parsed data as well as the sent command, vacuum chamber pressure, and the location of the output file and generates a .TDMS file containing the various inputs and other information about the last RPA sweep. Required inputs in boldface.

Figure A.10: **Main subVIs contained in RPA Save Files VI.** A screenshot of the RPA Save Files VI displays the built-in subVIs used to create, modify, and input data into the .TDMS file structure.

shows the TDMS File Viewer in LabView while reading an example RPA output file. The pop-up pauses the RPA control code GUI to allow the user to navigate the latest .TDMS file created by the "RPAsavefiles.vi."

A.4 RPAreadaverage.vi

The "RPAreadaverage.vi" program allows the user to plot and evaluate the output files generated by the RPA GUI and then to combine sets of I-V curves to generate time-averaged curves with error bars for each RV point. The code prompts the user to select a batch of .TDMS RPA output files from which averages and the standard deviation are calculated, and then writes out the properties of the files selected to a file. The program then prompts the user to evaluate the curve before selecting whether or not to save the averaged data set. If selected, the data set gets saved to a .TMDS file for plotting with MS Excel, MATLAB, C++, or a similar programming language. Figure A.12 displays a screen-shot of the "RPAreadaverage.vi" program.

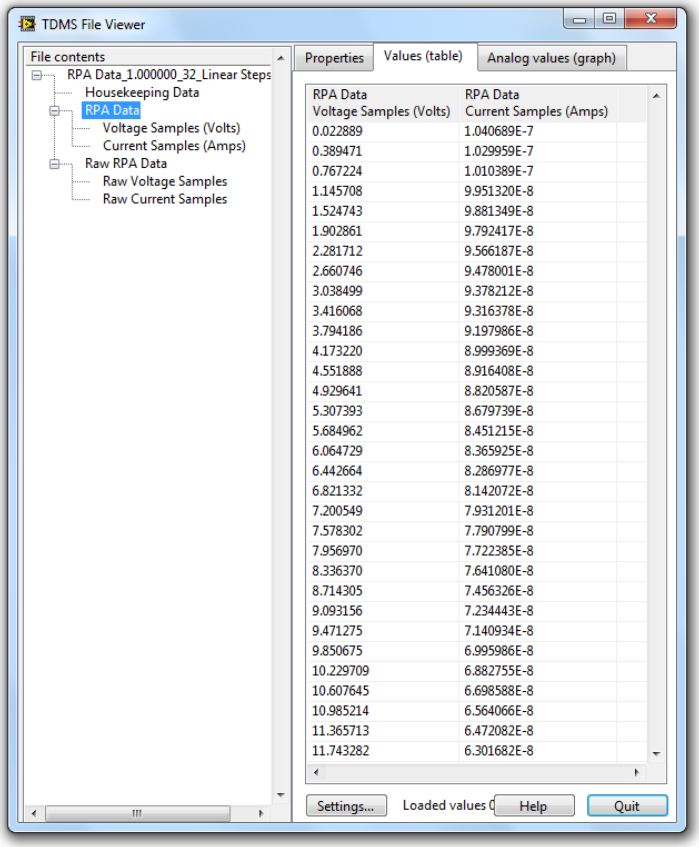

Figure A.11: **RPA Save Files VI TDMS File Viewer.** When enabled, the TDMS File Viewer pop-up pauses the RPA control code GUI to allow the user to navigate the latest .TDMS file created by the RPA Save Files VI.

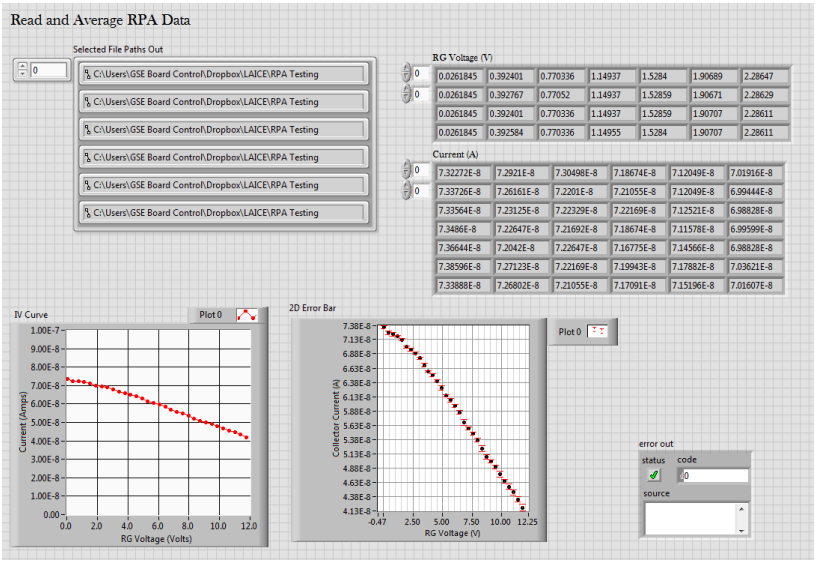

Figure A.12: **"RPAreadaverage.vi" program front panel.** The "RPAreadaverage.vi" program prompts the user to select a range to .TDMS RPA output files to average, compute the standard deviation, and output the statistical analysis and properties of the files selected.

Appendix B

RPA Board Extended Range

The RPA electronics were designed to set the 0-5 V input signal signal range and the instrumentation amplifier gain strategically such that the calibration of the instrument would encompass the entire specified input current plus some margin on each end of the range. The input current values outside of the normal operating range of the RPA were excluded from the calibration procedure, but the full signal range from 0 to 65535 decimal counts of 16-bit digital values is displayed here for completeness. Figures B.1, B.2, and B.3 show the results of the RPA flight board full range characterization. The blue lines on the plots signify the 5 V (65535 count) maximum of the signal.

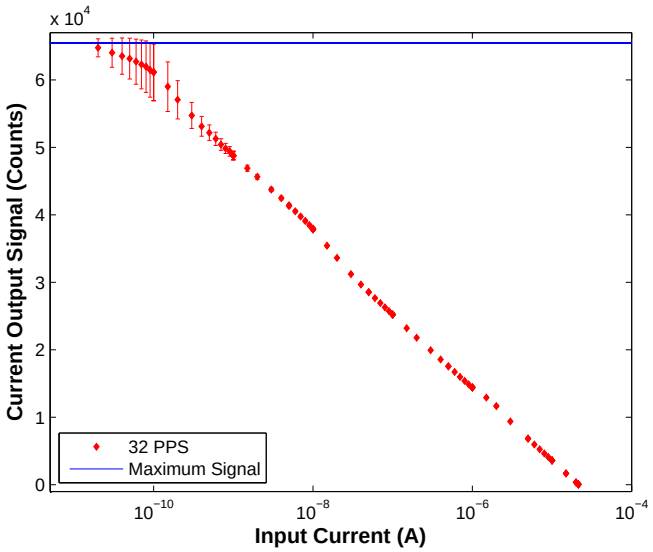

Figure B.1: **LAICE RPA 32 PPS calibration curve showing full range of input signal.** The calibration was performed over collector current input ranges of 10 pA to 21.5 μA. The output digital current signals read at the LabView console. The test was performed at atmosphere, room temperature, and inside the Space@VT vacuum chamber to limit EMI.

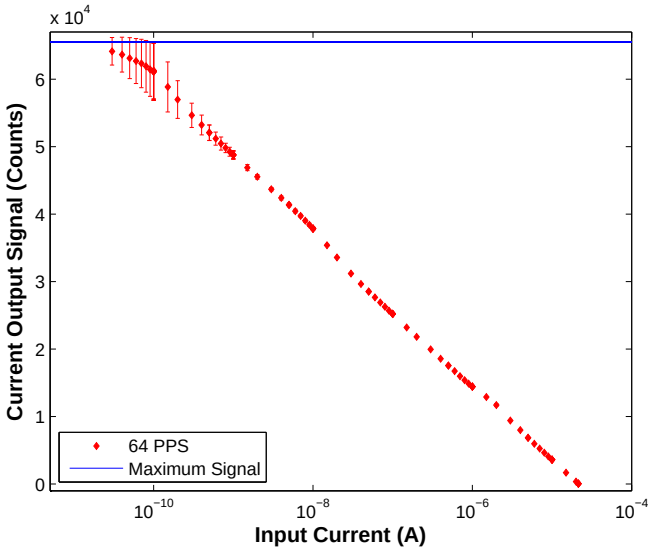

Figure B.2: **LAICE RPA 64 PPS calibration curve showing full range of input signal.** The calibration was performed over collector current input ranges of 20 pA to 21.5 μA. The output digital current signals read at the LabView console. The test was performed at atmosphere, room temperature, and inside the Space@VT vacuum chamber to limit EMI.

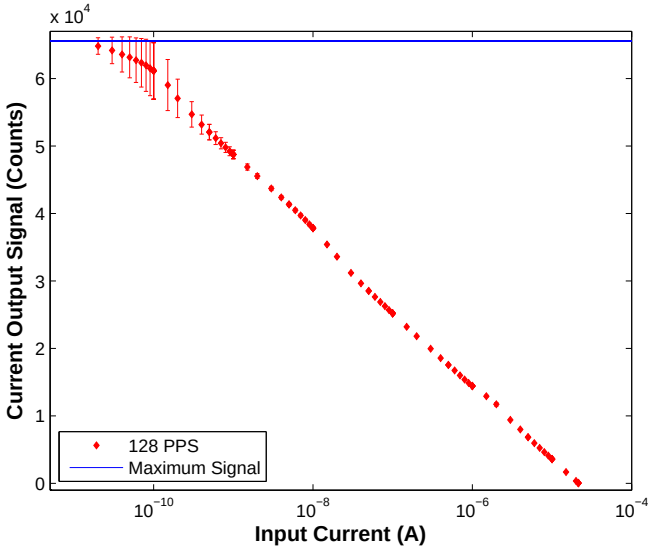

Figure B.3: **LAICE RPA 128 PPS calibration curve showing full range of input signal.** The calibration was performed over collector current input ranges of 10 pA to 21.5 μA. The output digital current signals read at the LabView console. The test was performed at atmosphere, room temperature, and inside the Space@VT vacuum chamber to limit EMI.

Appendix C

RPA Nominal Power Draw

Table C.1 shows the nominal power draw on the LAICE RPA sub-system (flight version). This test was performed at atmosphere and room temperature.

Table C.1: **LAICE RPA nominal power draw.** This test was performed at atmosphere and room temperature on the LAICE RPA flight system.

Signal	**Voltage (V)**	**Current Draw (A)**	**Power Draw (W)**
5V, 5VD, 5VC	5.0	0.020	0.100
-5V	-5.0	0.010	0.050
15V	15.0	0.016	0.240
-15V	-15.0	0.015	0.225
3.3VD	3.3	0.010	0.033
Total			**0.648**

Appendix D

Logarithmic-Polynomial Calibration Fit

Further evaluation of the logarithmic best-fit line from this text prompted a study of using a logarithmic-polynomial best fit line instead. Other kinds of curve-fitting were attempted which won't be discussed here, as the 6th-order logarithmic-polynomial fit using the Levenberg-Marquardt algorithm was found to have the highest accuracy with the measured calibration points. Equation D.1 shows the form of the resulting logarithmic-polynomial line.

$$f(x) = p6 \times log_{10}(x)^6 + p5 \times log_{10}(x)^5 + p4 \times log_{10}(x)^4 + p3 \times log_{10}(x)^3 + p2 \times log_{10}(x)^2 + p1 \times log_{10}(x) + b \quad \text{(D.1)}$$

Table D.1 shows the final logarithmic-polynomial fit coefficient values.

The logarithmic-polynomial fit has a coefficient of determination of $R^2 = 0.9999$. This is a

Table D.1: **Logarithmic-polynomial calibration fit coefficient values.** The values listed here correspond to the final fit coefficients of Equation D.1. This best fit line is plotted in Figure D.1.

Coefficient	**Value**
p6	28.77
p5	1210
p4	2.09×10^4
p3	1.89×10^5
p2	9.50×10^5
p1	2.49×10^6
b	2.66×10^6

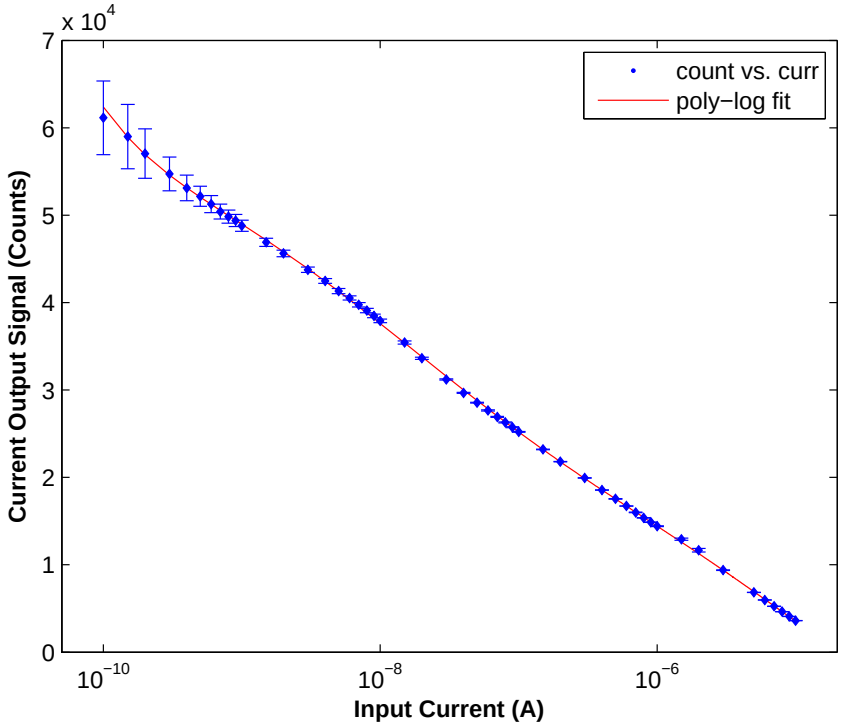

Figure D.1: **LAICE RPA calibration curve for a logarithmic-polynomial fit.** This calibration data was fit with a logarithmic-polynomial best fit line (shown). The calibration was performed over collector current input ranges of 100 pA to 10 μA. Digital current output signals were read at the LabView console. The test was performed at atmosphere, room temperature, and inside the Space@VT vacuum chamber to limit EMI.

slight improvement over the best case $R^2 = 0.9992$ for the logarithmic fit described in section 4.2. The maximum percent error from fit for any point in the logarithmic-polynomial fit is 3.5% whereas the logarithmic fit saw up to 18%. The high-end current ($> 1\mu$A) is more accurately calibrated in the logarithmic-polynomial fit compared to the logarithmic fit.

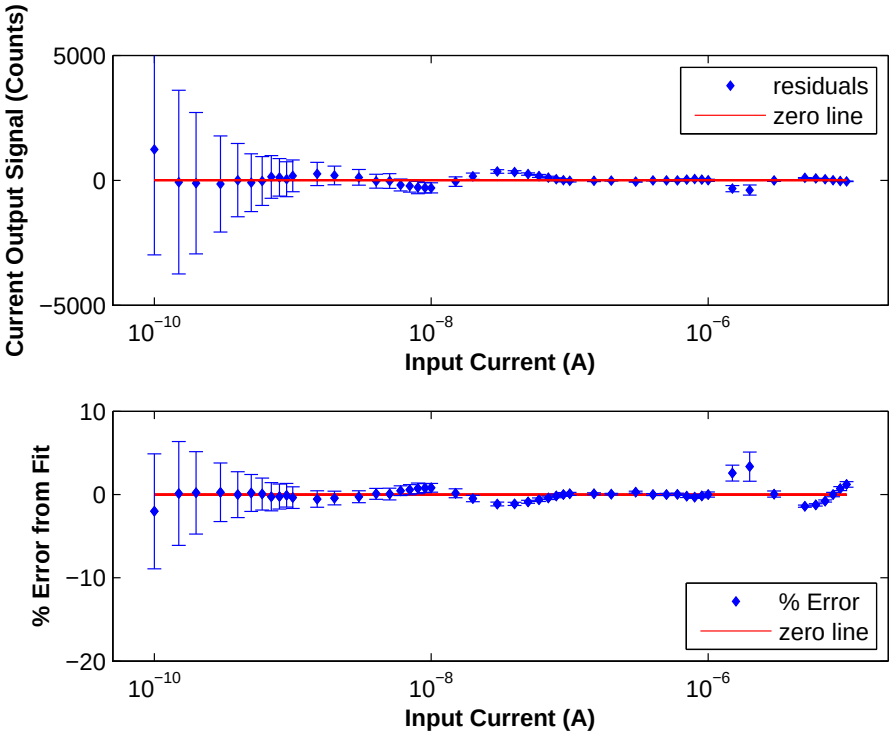

Figure D.2: **LAICE RPA electronics best fit line analysis for a logarithmic-polynomial fit.** The top subplot shows the residual analysis for the 32 PPS calibration with a logarithmic-polynomial best fit line. The error bars reference the standard deviation from the mean for that particular calibration point. The bottom subplot shows the percent error comparison of the measured calibration point to the logarithmic-polynomial best fit line.

Appendix E

RPA Board Schematics

All schematics appended in this chapter were first published in Lucy Fanelli. *Electronics for a versatile and robust retarding potential analyzer for use in nano-satellite platforms.* 2014. Masters thesis, Virginia Tech. Used under fair use, 2015.

They are included here for reference only.

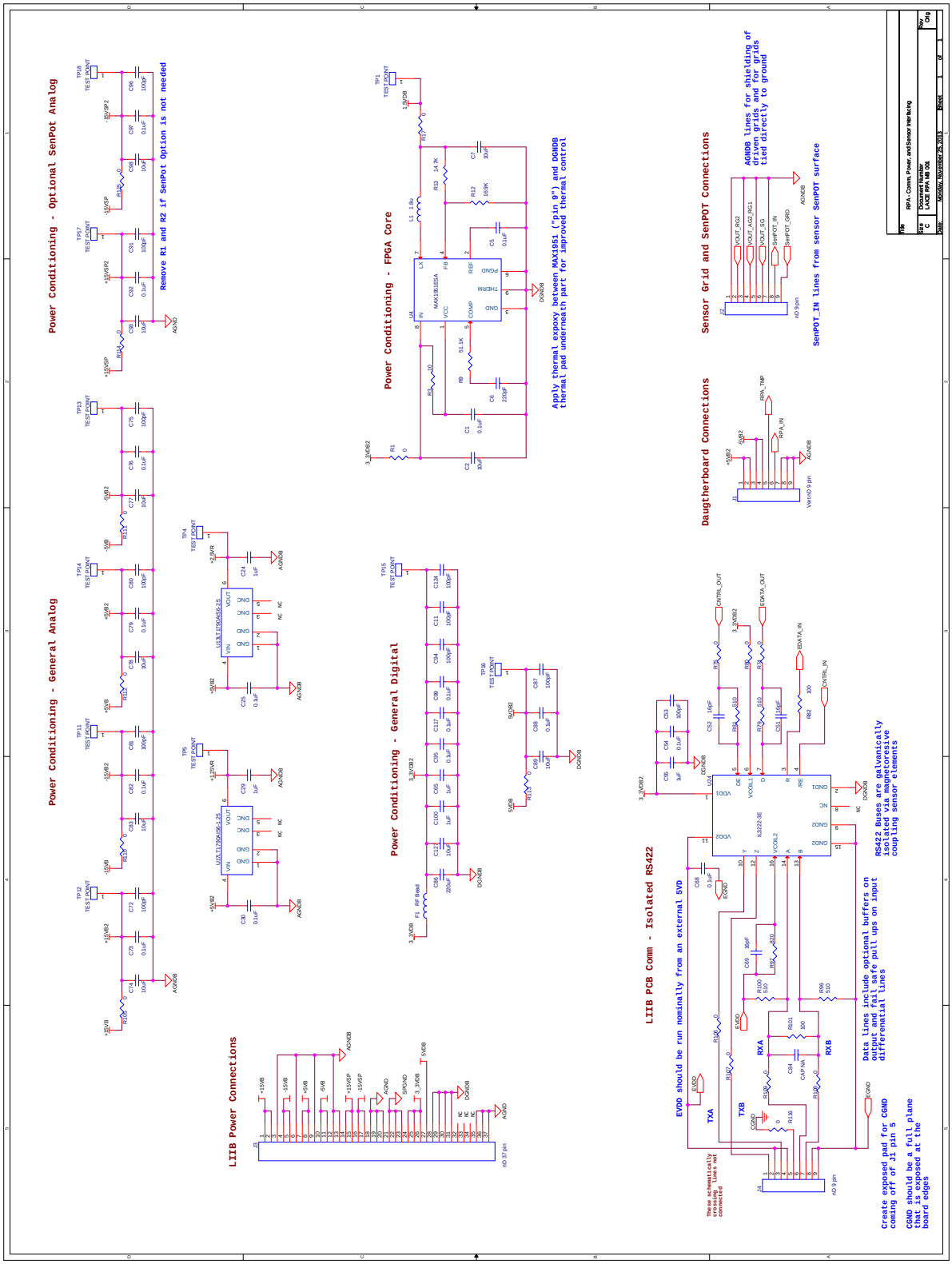
Power Conditioning - General Analog
Power Conditioning - Optional SenPot Analog
Remove R1 and R2 if SenPot Option is not needed
Power Conditioning - General Digital
Power Conditioning - FPGA Core
Apply thermal expoxy between MAX19951 ("pin 9") and DGNDB thermal pad underneath part for improved thermal control
Sensor Grid and SenPOT Connections
AGNDB lines for shielding of driven grids and for grids tied directly to ground
SenPOT_IN lines from sensor SenPOT surface
Daugtherboard Connections
LIIB PCB Comm - Isolated RS422
EVDD should be run nominally from an external 5VD
RS422 Buses are galvanically isolated via magnetoresive coupling sensor elements
Data lines include optional buffers on output and fail safe pull ups on input differential lines
Create exposed pad for CGND coming off of J1 pin 5
CGND should be a full plane that is exposed at the board edges
These schematically connected
LIIB Power Connections
RPA - Comm, Power, and Sensor Interfacing
Document Number
LACE RPA MB 008
Monday, November 26, 2012

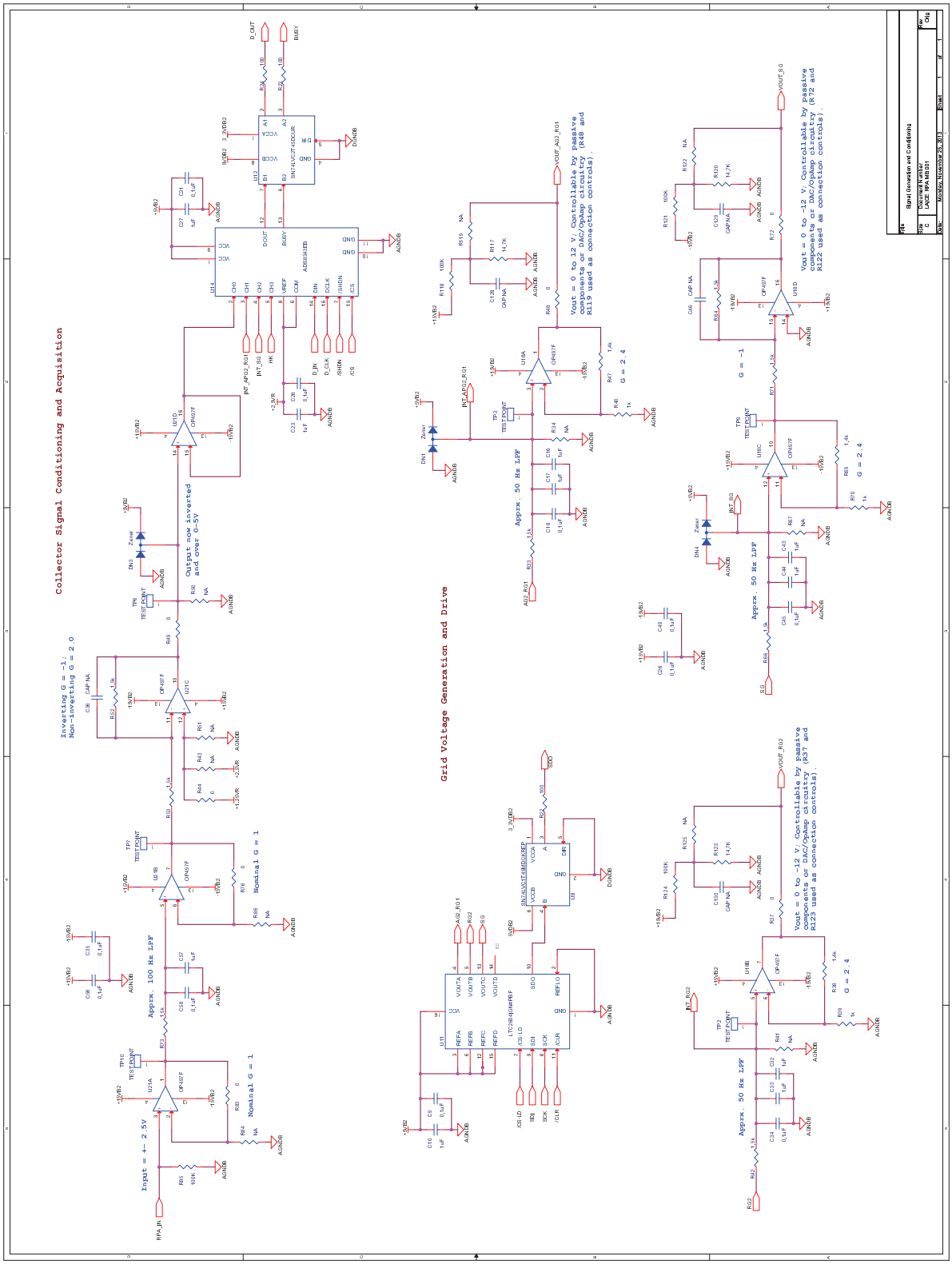
Collector Signal Conditioning and Acquisition
Inverting G = -1
Non-inverting G = 2.0
Output now inverted and runs 0-5V
Approx. 100 Hz LPF
Nominal G = 1
Input = +- 2.5V
Grid Voltage Generation and Drive
Approx. 50 Hz LPF
Vout = 0 to 12 V. Controllable by passive components or DAC/Opamp circuitry (R48 and R119 used as connection controls).
G = 2.4
Vout = 0 to -12 V. Controllable by passive components or DAC/Opamp circuitry (R72 and R122 used as connection controls).
G = -1
Vout = 0 to -12 V. Controllable by passive components or DAC/Opamp circuitry (R37 and R123 used as connection controls).
Signal Generation and Conditioning
Monday, November 26, 2012

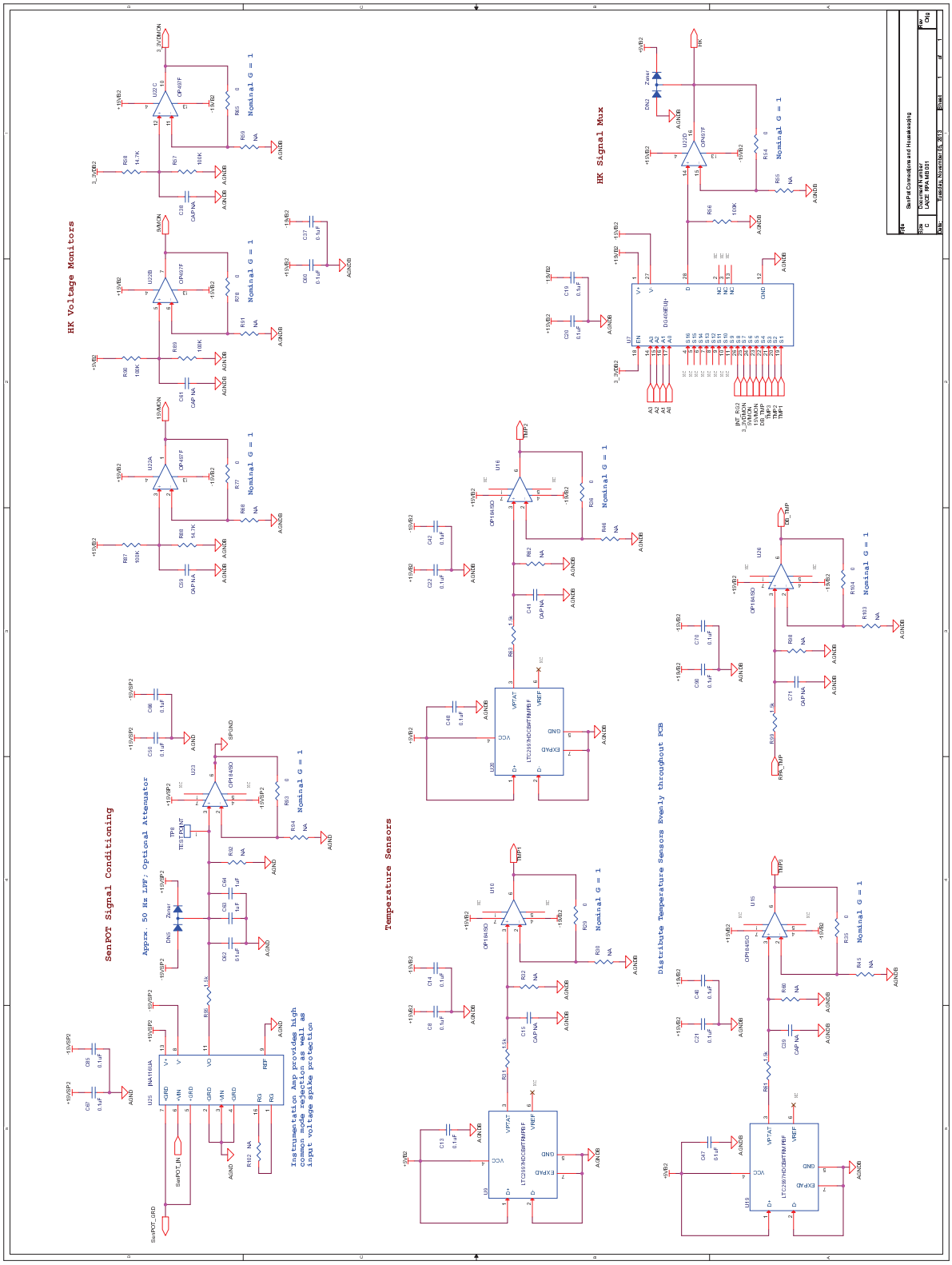
HK Voltage Monitors
HK Signal Mux
SenPOT Signal Conditioning
Approx. 50 Hz LPF; Optional Attenuator
Instrumentation Amp provides high common mode rejection as well as input voltage spike protection
Temperature Sensors
Distribute Temperature Sensors Evenly throughout PCB
Nominal G = 1
Title
Size C
Date: Tuesday, November 05, 2013
Sheet

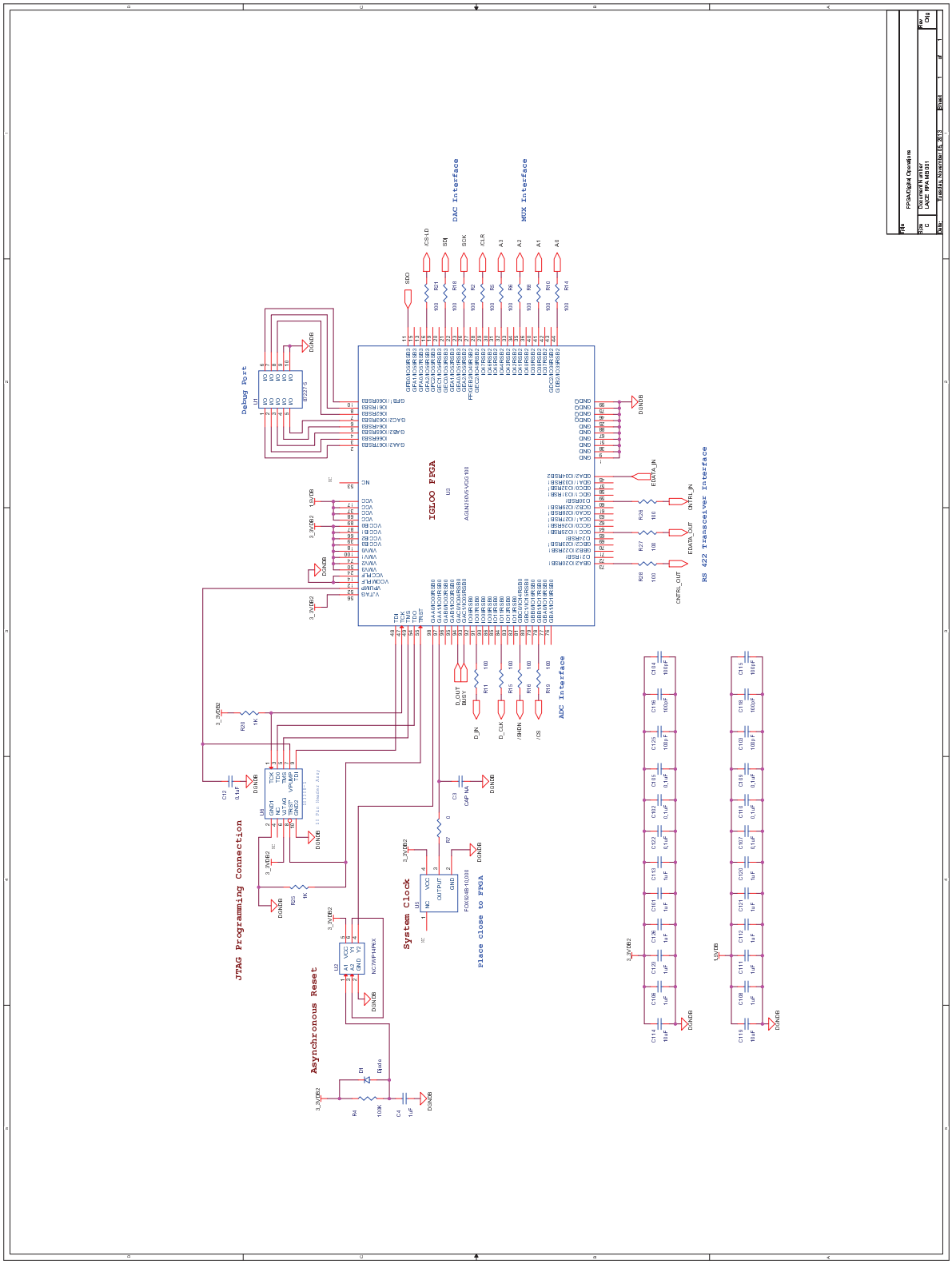
IGLOO FPGA
DAC Interface
MUX Interface
ADC Interface
RS 422 Transceiver Interface
Debug Port
JTAG Programming Connection
System Clock
Asynchronous Reset
Place close to FPGA

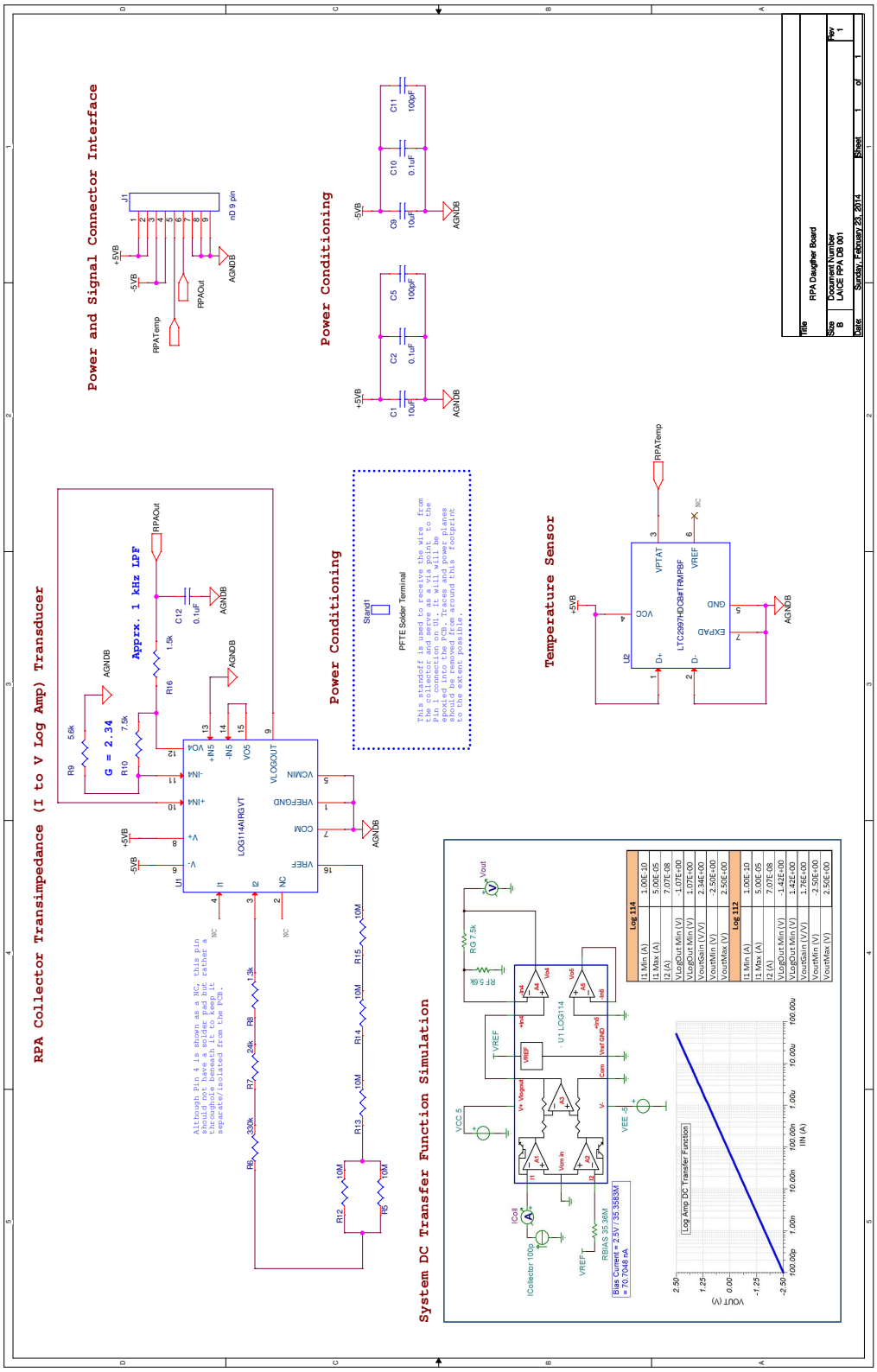
RPA Collector Transimpedance (I to V Log Amp) Transducer
Power and Signal Connector Interface
Power Conditioning
Power Conditioning
Temperature Sensor
System DC Transfer Function Simulation
Appx. 1 kHz LPF
G = 2.34
LOG114AIRGVT
LTC2997HDC8#TRMPBF
PFTE Solder Terminal
RPA Daughter Board
Document Number
LACE RPA DB 001
Sunday, February 23, 2014